Ab initio calculation of the attempt frequency of oxygen diffusion in pure and samarium doped ceria

Julius Koettgen,[*a] Tobias Zacherle,[a] Steffen Grieshammer,[ab] and Manfred Martin[*abcd]

The rate of oxygen ion jumps in a solid oxide depends not only on the activation energy but also on the pre-exponential factor of diffusion. In order to allow a fully *ab initio* prediction of the oxygen ion conductivity in pure and samarium doped ceria we calculated the attempt frequency for an oxygen ion jump from first principles combining DFT+U, NEB, phonon calculations and the transition state theory. Different definitions of the jump attempt frequency are presented. The equivalence of the Eyring and the Vineyard method is shown without restriction to the Gamma point. Convergence checks of the phonon mesh reveal that the common reduction to the Gamma point is not sufficient to calculate the attempt frequency. Calculations of Sm doped ceria revealed an increase of the prefactor. The attempt frequency for the constant pressure case in quasi-harmonic approximation is larger than the attempt frequency at constant volume in harmonic approximation. The calculated electronic energies, enthalpies and entropies of migration are in agreement with experimental diffusion coefficients and activation energies.

1 Introduction

The increasing use of renewable energy sources like wind and solar power highlights the importance of energy conversion and storage. Solid oxide fuel cells (SOFC) provide high energy conversion efficiency and excellent fuel flexibility and are therefore a promising candidate for future energy applications. For good performance, an electrolyte with high oxygen ion conductivity is required. Potential materials are fluorite-structured oxides, such as doped zirconia (ZrO_2) and doped ceria (CeO_2), the latter favorably allowing a reduction of the operating temperature from 900 °C to 600 °C. Pure cerium oxide itself is not a good ionic conductor.[1] In contrast doping with lower valent oxides like rare-earth oxides creates oxygen vacancies which results in a significant increase in oxygen ion conductivity. In particular, doping with samarium oxide (Sm_2O_3) leads to high conductivities as revealed by impedance spectroscopy experiments.[2]

The ionic conductivity σ_i of the oxygen ions ($i = O^{2-}$) or vacancies ($i = V_O^{\bullet\bullet}$) is proportional to their squared charge $z_i^2 e^2$, concentration n_i and mechanical mobility b_i (Eq. 1). The mobility is related to the diffusion coefficient D_i by the classical Einstein relation for non-interacting defects with the Boltzmann constant

k_B and the absolute temperature T.[†] Both diffusion coefficients ($D_{O^{2-}}$ and $D_{V_O^{\bullet\bullet}}$) depend on the weighted mean jump rate of all oxygen ions ($\overline{\Gamma}_{O^{2-}}$) or vacancies ($\overline{\Gamma}_{V_O^{\bullet\bullet}}$) to one nearest neighbor site. In this work, jumps to other lattice sites are neglected according to Nakayama and Martin.[4] In Eq. 1 l is the jump distance and γ is the geometrical factor, which includes the number of jump sites n_p and the dimension of diffusion d and is $\gamma = \frac{n_p}{2d} = 1$ in a primitive cubic lattice, e.g. the oxygen sublattice in ceria.[5,6] The jump rate can be described by an Arrhenius equation (Eq. 2) with the activation enthalpy at constant pressure $\Delta H_a(p, T)$. The activation enthalpy describes the experimentally determined dependence of the diffusion coefficient on temperature and can be calculated from the slope of a plot $\ln \overline{\Gamma}_i$ versus $1/T$.

$$\sigma_i = n_i \cdot z_i^2 e^2 \cdot b_i, \text{ where } b_i = \frac{D_i}{k_B T} \text{ and } D_i = \gamma l^2 \cdot \overline{\Gamma}_i. \quad (1)$$

$$\overline{\Gamma}_i(p, T) = \overline{v}_{\exp,i}(p, T) \cdot e^{-\frac{\Delta H_a(p,T)}{k_B T}} \quad (2)$$

Therefore, the pre-exponential factor for diffusion $D_{0,i} = \gamma l^2 \cdot \overline{v}_{\exp,i}(p, T)$ depends on the frequency $\overline{v}_{\exp,i}(p, T)$. The latter can be interpreted as *mean experimental attempt frequency* of all oxygen vacancies or oxygen ions to jump to one nearest neighbor site at constant pressure. It should be noted that several definitions of the term 'attempt frequency' exist, which will be discussed in section 2. Naturally, deviations in the activation en-

[a] Institute of Physical Chemistry, RWTH Aachen University, Landoltweg 2, 52056 Aachen, Germany. Fax: +49-241-80-92128; Tel: +49-241-80-94712; E-mail: julius.koettgen@rwth-aachen.de, martin@rwth-aachen.de

[b] Helmholtz-Institut Münster (IEK-12), Forschungszentrum Jülich GmbH, Corrensstr. 46, 48149 Münster, Germany.

[c] JARA-Energy, Forschungszentrum Jülich and RWTH Aachen University, Germany.

[d] JARA-HPC, Forschungszentrum Jülich and RWTH Aachen University, Germany.

[†] For high defect concentrations an 'exact Nernst-Einstein' relation using the chemical potential can be applied.[3]

This journal is © the Owner Societies 2017

Phys. Chem. Chem. Phys., 2017, 19, 9957 | 1–17 | 1

thalpy, which appears in the exponential term, possess a stronger influence on the jump rate than deviations in the attempt frequency.

The conductivity of an oxygen ion conductor (Eq. 1) can be defined for both oxygen ions and vacancies whereat both conductivities are equal in value. Likewise, the absolute value of the oxygen ions charge is equal to the Kröger-Vink charge of the oxygen vacancies. Therefore, the diffusion coefficients of ions $D_{O^{2-}}$ and vacancies $D_{V_O^{\bullet\bullet}}$ differ according to

$$D_{O^{2-}} = \frac{n_{V_O^{\bullet\bullet}}}{n_{O^{2-}}} D_{V_O^{\bullet\bullet}}, \qquad (3)$$

with the concentration of oxygen ions $n_{O^{2-}}$ and oxygen vacancies $n_{V_O^{\bullet\bullet}}$ (cf. 'jump balance'). The same applies to the mean jump rate $\overline{\Gamma}_i$ and the mean attempt frequency $\overline{v}_{exp,i}(p,T)$. In a pure ceria crystal with isolated defects, all oxygen vacancies have the same attempt frequency $\overline{v}_{exp,V_O^{\bullet\bullet}} = v_{exp,V_O^{\bullet\bullet}}$ where $v_{exp,V_O^{\bullet\bullet}}$ is the attempt frequency for the jump of one individual oxygen ion to a vacant lattice site. This is the elementary frequency for a jump process where both the jumping oxygen vacancy and the jumping oxygen ion have the same jump attempt frequency and which is calculated in this work. In the transition state theory, attempt frequencies of individual defects are calculated. Since oxygen ions can only jump when a neighboring vacancy exists, the mean attempt frequency of all oxygen ions $\overline{v}_{exp,O^{2-}}$ depends on the fraction of oxygen vacancies. We assume that the attempt frequency of an oxygen vacancy $v_{exp,V_O^{\bullet\bullet}}$ is not influenced by other vacancies. Therefore, the attempt frequency and the diffusion coefficient of the oxygen ions increase with increasing oxygen vacancy fraction according to Eq. 3.

In doped ceria, a variety of ionic configurations occurs, which leads to a variety of jump environments and possibly different local attempt frequencies. As a macroscopic property, the mean experimental attempt frequency $\overline{v}_{exp,i}(p,T)$ is influenced by all local attempt frequencies that affect the diffusion.

The ionic conductivity in ceria can be simulated by means of molecular dynamics (MD) using pair potentials[7–12] or by kinetic Monte Carlo simulations (KMC) using empirical[13] or *ab initio* calculations[4,14–17] for the activation barrier (migration energy) for each occurring jump. In all these KMC studies 'a typical value' (mostly 10^{13} s^{-1}) for the attempt frequency for all ionic configurations was applied. For praseodymium doped ceria, Dholabhai *et al.* calculated the attempt frequency by means of density functional theory with an Hubbard U parameter (DFT+U) resulting in $5 \cdot 10^{12}$ s^{-1} for one of many possible ionic configurations.[18] However, a Vineyard approximation was applied considering only the Gamma point. As mentioned before, it was assumed that the attempt frequency is constant for different configurations. Attempt frequencies for different ionic configurations are rarely calculated. Tarancón *et al.* used classical molecular dynamics (MD) to indirectly calculate attempt frequencies for $Ce_{0.92}Gd_{0.08}O_{1.96}$ resulting in $(5.4 \pm 0.3) \cdot 10^{12}$ s^{-1} for jumps through an edge formed either by two host cations (Ce-Ce edge, see Fig. 1) or one dopant and one host cation (Ce-Gd edge).[10]

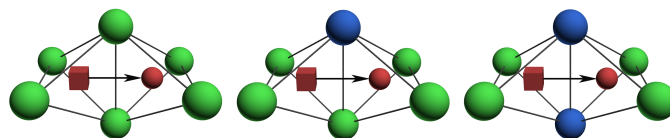In order to allow a fully *ab initio* prediction of the oxygen ion

Fig. 1 Possible migration edge configurations in samarium doped ceria. Ce-Ce edge (left), Ce-Sm edge (middle) and Sm-Sm edge (right). Cerium ions (green), samarium ions (blue), oxygen ions (red spheres) and oxygen vacancies (red boxes).

conductivity, in this work we calculated the attempt frequencies for oxygen ion jumps in pure and doped ceria for different configurations from first principles combining DFT, the nudged elastic band method (NEB) and phonon calculations.

The migration of oxygen vacancies in fluorite structured ceria is considered between adjacent tetrahedral oxygen sites[4] in (100) direction with the experimental jump distance $l = 2.7055$ Å given by half of the unit cell length.[19] Along this migration pathway two cations form a 'migration edge'. In pure CeO_2, only cerium ions are at the migration edge, while doping with samarium oxide leads to configurations with one or two Sm ions at the migration edge (see Fig. 1). Jumps through a Ce-Ce, Ce-Sm or Sm-Sm edge were explicitly calculated in this work. For KMC simulations, the migration energies and the attempt frequencies must be known for all occurring configurations containing multiple Sm dopants and oxygen vacancies at various positions. The migration energies of all possible configurations can be calculated combining three explicit migration edge energies with association energies between the migrating oxygen vacancy and the other adjacent defects according to a pair interaction model proposed earlier.[20] The attempt frequencies of the three edge configurations are assumed to be representative for all possible migration configurations.

It is known that under oxygen poor conditions ceria can be reduced leading to the formation of polarons[21,22] and a number of theoretical studies has been dedicated to this subject.[17,23–27] However, we restrict our simulations to conditions were the number of polarons is much smaller than the dopant level and can thus be neglected.

The paper is organized as follows: In section 2, we introduce the transition state theory according to Eyring and Vineyard and show the equivalence of their results without restriction to the Gamma point. In section 3, computational details according to the general computational setup and the phonon calculations are described. In section 4, we present our results for the attempt frequency in pure ceria depending on the phonon mesh and the influence of doping with samarium as well. The calculated attempt frequencies for constant volume are transformed to constant pressure. Finally, we compare the calculations with experiments. In section 5, we give a short summary.

2 Theory

2.1 Historical developments concerning the rate constant

Reaction rate theory was majorly influenced by Arrhenius,[28] Trautz and Lewis,[29,30] Eyring[31] and Vineyard.[32] The Arrhenius equation[28] (Eq. 2), originally formulated in 1889 for the temper-

2 | 1–17 | Phys. Chem. Chem. Phys., 2017, **19**, 9957

This journal is © the Owner Societies 2017

ature dependent rate constant of a chemical reaction, assumes that a minimum amount of activation energy at constant volume (or enthalpy at constant pressure) is necessary to transform reactants into products. Thus, the reaction rate is proportional to the product of a pre-exponential factor and the probability an activated state occurs. While Arrhenius assumed a constant prefactor, about 25 years later, Max Trautz and William Lewis[29,30] proposed a minor temperature dependence of the pre-exponential factor. According to their collision theory, a reaction occurs if the kinetic energy along the line-of-centers at contact exceeds a specific value.[33] However, other degrees of freedom can also contribute to the formation of the activated state,[34] and discrepancies between theoretical and experimental results were observed.

2.2 Transition state theory according to Eyring

In the year 1935 Eyring[31] published an essential contribution to the transition state theory or absolute-rate theory. He proposed between initial state (IS) and transition state (TS) a quasi-equilibrium $IS \rightleftharpoons TS$. The corresponding equilibrium constant is $K = c_{TS}/c_{IS}$ where c_{TS} and c_{IS} are the concentrations of the reactants in both respective states. Once the transition state configuration is reached, every complex decomposes to the product (P) with the decomposition frequency ν_d, $IS \rightleftharpoons TS \overset{\nu_d}{\to} P$. Then, the reaction rate for the formation of the product P can be written as

$$\text{reaction rate} = \nu_d c_{TS} = \underbrace{\nu_d K}_{k} c_{IS}. \tag{4}$$

Here k is the reaction rate constant. A transmission factor $\kappa \leq 1$ could be included in Eq. 4 to account for 'return jumps', though it cannot be evaluated in the frame of the transition state theory.[‡] Hence, the classical transition state theory is an upper bound to the true reaction rate.[41]

The equilibrium constant K in Eq. 4 can be expressed by the partition functions of the initial state Z_{IS} and the transition state Z_{TS}.[42] Both of them can be written as a product of an electronic partition function Z_{el} and a vibrational partition function Z_{vib} assuming no coupling between vibrational and electronic excitation (Eq. 5). For temperatures far below the Fermi temperature, the electronic partition function is primarily determined by the electronic ground state. Therefore, the ratio of the electronic partition functions results in $\exp\left(-\frac{\Delta E_{el}^0}{k_B T}\right)$ where ΔE_{el}^0 is the electronic energy difference between the activated complex and the reactants for temperatures far below the Fermi temperature. This quantity is typically obtained in *ab initio* calculations at absolute zero.

$$K = \frac{Z_{TS}}{Z_{IS}} = \frac{Z_{TS,vib}}{Z_{IS,vib}} \frac{Z_{TS,el}}{Z_{IS,el}} = \frac{Z_{TS,vib}}{Z_{IS,vib}} e^{-\frac{\Delta E_{el}^0}{k_B T}} \tag{5}$$

Until now, all transition state related properties like the concentrations c_{TS}, the equilibrium constant K, and the vibrational partition function $Z_{TS,vib}$ contained the decomposition vibration. However, the vibrational mode, which corresponds to the decomposi-

[‡] A 'return jumps' rate is taken into account by the Kramers approach,[35] and the short-memory augmented-rate theory (SM-ART) framework of Toller et al.[34,36–40]
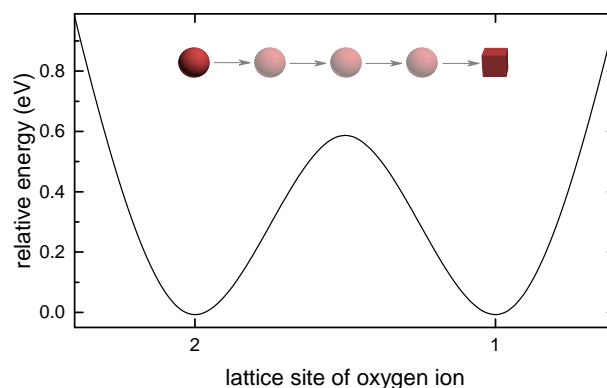
Fig. 2 Sketch of the electronic energy profile for an oxygen jump in pure ceria according to Eq. 7.

tion vibration, has to be excluded from these properties for the calculation of the free energy. Therefore, the partition function for the critical vibration can be separated from the vibrational partition function according to $Z_{TS,vib} = \frac{k_B T}{h \nu_d} Z'_{TS,vib}$.[§] Here, $Z'_{TS,vib}$ is the vibrational partition function for all normal coordinates except the decomposition vibration, similar to a modified equilibrium constant $K' = c'_{TS}/c_{IS} = (h\nu_d)/(k_B T) K$. Therefore, the transition state partition function $Z'_{TS,vib}$ has one degree of freedom less than the initial state partition function $Z_{IS,vib}$. The final expression for the reaction rate constant is

$$k = \frac{k_B T}{h} \frac{Z'_{TS,vib}}{Z_{IS,vib}} e^{-\frac{\Delta E_{el}^0}{k_B T}}. \tag{6}$$

Equation 6 can be applied to the diffusion process as follows: The migration of an oxygen ion $O_O^\times$ from a lattice site 2 to a lattice site 1 can be described by the following quasi-chemical reaction:

$$V_{O1}^{\bullet\bullet} + O_{O2}^\times \rightleftharpoons V_{O1}^{\bullet\bullet} + O_{TS}'' + V_{O2}^{\bullet\bullet} \to O_{O1}^\times + V_{O2}^{\bullet\bullet}. \tag{7}$$

In the initial state (IS), the oxygen ion occupies lattice site 2, while the oxygen vacancy occupies a neighboring lattice site 1. In the transition state (TS), the oxygen ion is located on the saddle point between both empty lattice sites 1 and 2. Finally, in the product state P, the oxygen ion occupies lattice site 1 and the vacancy occupies lattice site 2. The corresponding electronic energy profile is shown in Fig. 2. Comparing Eqs. 7 and 4 indicates that the jump rate Γ for this elementary site exchange process corresponds to the reaction rate constant k discussed before.

[§] The decomposition vibration can be described as classical harmonic oscillator where the weighted number of states consists of the kinetic and potential energy weighted by the Boltzmann factor, integrated over phase space and 'arbitrarily' divided by the Planck constant. This is similar to a quantum harmonic oscillator without zero point energy and in high temperature limit ($k_B T \gg h\nu_d$). Instead of describing the decomposition motion as a vibration, a translational degree of freedom can be used. Then, the reaction rate can be defined as product of the concentration of the transition state c_{TS}, the translational partition function for the particle in an one-dimensional box $Z_{translational} = \frac{\sqrt{2\pi m k_B T}}{h}\delta$ with the box length δ and the effective mass associated with the translation along the reaction coordinate m. This modified transition state concentration is multiplied with the mean velocity given by an one-dimensional Maxwell-Boltzmann distribution $\bar{v} = \sqrt{\frac{k_B T}{2\pi m}}$ and the inverse box length $1/\delta$.[34,42–44]

The partition functions $Z'_{\text{TS,vib}}$ and $Z_{\text{IS,vib}}$ in Eq. 6 can be described by means of the quantum harmonic oscillator excluding the decomposition frequency (see next subsection). For a system at constant volume, both partition functions correlate with the free energy F according to $F(V,T) = -k_{\text{B}}T \ln Z(V,T)$. Introducing the vibrational free energy difference of initial and transition state, $\Delta F_{\text{vib}} = F_{\text{vib,TS}} - F_{\text{vib,IS}}$, finally the Eyring formula for the jump rate at constant volume (Eq. 8) is obtained.

$$\Gamma(V,T) = \underbrace{\frac{k_{\text{B}}T}{h} e^{-\frac{\Delta F_{\text{vib}}(V,T)}{k_{\text{B}}T}}}_{\nu_0(V,T)} e^{-\frac{\Delta E_{\text{el}}^0(V)}{k_{\text{B}}T}} \qquad (8)$$

Similar to the Arrhenius equation (Eq. 2), the Eyring formula (Eq. 8) is a product of an attempt frequency, here $\nu_0(V,T)$, and an exponential term containing the electronic energy difference, $\Delta E_{\text{el}}^0(V)$, whereat the latter is temperature independent. The definition of the attempt frequency according to Eyring in Eq. 8 is commonly used in literature since $\nu_0(V,T)$ is independent of temperature at high temperatures (see section 4) and can be easily used in combination with the electronic energy difference ΔE_{el}^0 which is the standard result for *ab initio* calculations.

In addition, the total free energy difference between transition state and initial state can be used, again, with the assumption of no excited electronic states for temperatures far below the Fermi temperature

$$\Delta F = \Delta E_{\text{el}}^0 + \underbrace{\Delta E_{\text{vib}} - T\Delta S_{\text{vib}}}_{\Delta F_{\text{vib}}}, \qquad (9)$$

where ΔE_{vib} is the vibrational energy difference and ΔS_{vib} the entropy difference of initial and transition state. Thus, Eq. 8 can be written as

$$\begin{aligned}\Gamma(V,T) &= \frac{k_{\text{B}}T}{h} e^{-\frac{\Delta F(V,T)}{k_{\text{B}}T}} \\ &= \underbrace{\frac{k_{\text{B}}T}{h} e^{\frac{\Delta S_{\text{vib}}(V,T)}{k_{\text{B}}}} e^{-\frac{\Delta E_{\text{vib}}(V,T)}{k_{\text{B}}T}}}_{\nu_0(V,T)} e^{-\frac{\Delta E_{\text{el}}^0(V)}{k_{\text{B}}T}}.\end{aligned} \qquad (10)$$

Until now, we assumed that the volume of the solid is constant during the migration, while experiments are usually performed at a constant pressure of $p = 1$ bar. This leads to a change in volume during the jump of the oxygen ion from the initial to the transition state, which is limited as atomic displacements in a solid proceed with the speed of sound.[45–47] Nevertheless, the attempt frequency can be calculated at constant pressure. Similar to Eqs. 4 and 6 the reaction rate is

$$\text{reaction rate} = \nu_{\text{d}} \underbrace{\frac{k_{\text{B}}T}{h\nu_{\text{d}}} c'_{\text{TS}}}_{c_{\text{TS}}} = \underbrace{\nu_{\text{d}} \frac{k_{\text{B}}T}{h\nu_{\text{d}}} K'}_{k} c_{\text{IS}}. \qquad (11)$$

Therefore, the activated states with the concentration c_{TS} decompose to the product with the unknown decomposition frequency ν_{d}, while for the modified concentration c'_{TS} the prefactor $k_{\text{B}}T/h$ is e.g. $1.9 \cdot 10^{13}$ s^{-1} at 900 K. Using the change in standard Gibbs free energy between transition and initial state $\Delta G = -k_{\text{B}}T \ln K'$

according to the Van't Hoff isotherm results in the jump rate:[44,48]

$$\Gamma(p,T) = \frac{k_{\text{B}}T}{h} e^{-\frac{\Delta G(p,T)}{k_{\text{B}}T}} = \underbrace{\frac{k_{\text{B}}T}{h} e^{\frac{\Delta S_{\text{vib}}(p,T)}{k_{\text{B}}}}}_{\nu_{\text{s}}(p,T)} e^{-\frac{\Delta H(p,T)}{k_{\text{B}}T}}, \qquad (12)$$

with the Gibbs free energy difference $\Delta G = \Delta H - T\Delta S_{\text{vib}}$ while assuming no change in the electronic entropy. Here, all thermodynamic quantities are in standard state i.e. their pure form at 1 bar. Of course, this derivation can also be used for the constant volume case. The enthalpy of migration at constant pressure is $\Delta H = \Delta E_{\text{el}}^0 + \Delta E_{\text{vib}} + p\Delta V$. In this work, the electronic energy difference ΔE_{el}^0, the attempt frequency $\nu_0(p,T)$, the vibrational energy difference ΔE_{vib} and the migration volume ΔV are calculated for a system at zero pressure (see section 4) which is a good approximation for $p = 1$ bar. The resulting pressure-volume work of migration $p\Delta V$ with $p = 1$ bar is rather small (about 10^{-6} eV) and will be neglected here:[41]

$$\Gamma(p,T) = \underbrace{\frac{k_{\text{B}}T}{h} e^{\frac{\Delta S_{\text{vib}}(p,T)}{k_{\text{B}}}} e^{-\frac{\Delta E_{\text{vib}}(p,T)}{k_{\text{B}}T}}}_{\nu_0(p,T)} e^{-\frac{\Delta E_{\text{el}}^0(p)}{k_{\text{B}}T}}. \qquad (13)$$

While theoretical calculations use the enthalpy of migration ΔH to calculate the jump rate according to Eq. 12, experimental measurements rely on the activation enthalpy ΔH_{a} (Eq. 2). Using the definition of the activation enthalpy $\Delta H_{\text{a}} = k_{\text{B}}T^2 (\partial \ln \Gamma(p,T)/\partial T)$ according to Eq. 2 in Eq. 12, the relation between both energies can be formulated by $\Delta H_{\text{a}} = \Delta H + k_{\text{B}}T$ leading to

$$\Gamma(p,T) = \underbrace{\frac{k_{\text{B}}T}{h} e^{\frac{\Delta S_{\text{vib}}(p,T)}{k_{\text{B}}}} e^1}_{\nu_{\text{exp},V_{\text{O}}^{\bullet\bullet}}(p,T)} e^{-\frac{\Delta H_{\text{a}}(p,T)}{k_{\text{B}}T}}. \qquad (14)$$

In theoretical calculations, the attempt frequency $\nu_0(p,T)$ according to the Eyring theory is combined with the electronic energy difference at zero temperature $\Delta E_{\text{el}}^0(p,T)$ to calculate the reaction rate (Eq. 13). In experiments, the measured quantities are the experimental attempt frequency $\nu_{\text{exp},V_{\text{O}}^{\bullet\bullet}}(p,T)$ and the activation enthalpy $\Delta H_{\text{a}}(p,T)$ (Eq. 14). Therefore, both equations cannot be directly compared, in general. However, for ceria and Sm doped ceria the vibrational energy ΔE_{vib} is calculated in this work to be approximately $-k_{\text{B}}T$ at high temperature. This corresponds exactly to the value of the missing vibrational degree of freedom of the transition state that consists of kinetic and potential energy. As a result, calculated attempt frequencies $\nu_0(p,T)$ and experimental attempt frequencies $\nu_{\text{exp},V_{\text{O}}^{\bullet\bullet}}(p,T)$ can be directly compared. In conductivity and diffusion experiments, only a macroscopic attempt frequency $\overline{\nu}_{\text{exp},V_{\text{O}}^{\bullet\bullet}}(p,T)$ and activation enthalpy can be extracted. Hence, calculated and experimental attempt frequencies can only be directly compared according to Eq. 2 if all jump environments are equivalent.

The attempt frequency is commonly assumed to be 'a typical value' in the range of $10^{12} - 10^{13}$ s^{-1}.[5,49,50] This is based on the assumption that the vibrational partition functions of initial and activated state in Eyring's formula (Eq. 6) are similar[41] resulting in the frequency $k_{\text{B}}T/h$ that is $6.2 \cdot 10^{12}$ s^{-1} at room temperature and $1.9 \cdot 10^{13}$ s^{-1} at 900 K.

2.3 Transition state theory according to Vineyard

Vineyard[32] adapted Eyring's concept to the movement of defects in solids in 1957. Even though only one atom jumps in the elementary process, the movement of defects is essentially a many-body process since the migrating defect interacts with neighboring atoms. The absolute rate theory is in its general form already a many-body process; however, most authors had oversimplified solid state processes to one-body models or assumed that all surrounding atoms are fixed. Vineyard avoided these reductions. A hyper-surface is defined, which passes through the transition state and is orthogonal to contours of equal potential energy separating the initial and the final jump position. The jump rate is given by the ratio of representative points on one side of the hyper-surface to the number of points crossing the hyper-surface from just this site. Any representative point of the system that reaches the hyper-surface with finite velocity will unavoidably cross to the product site. This corresponds to the transition state in the Eyring theory, which always decomposes to the product. Using the theory of small vibrations, a high-temperature approximation and a reduction to the Gamma Point, the attempt frequency can be calculated by the Vineyard formula

$$
v_0 = \frac{\prod\limits_{i}^{N} v_i}{\prod\limits_{j}^{N-1} v_j},
\tag{15}
$$

where v_i and v_j are the normal frequencies for vibration in the initial and transition state at the Gamma point, respectively. Thereby, the product for the initial state features one additional normal frequency compared to the transition state product. Limitations of the Vineyard theory were illustrated by Bennett[51,52] and Da Fano *et al.*[53] A similar solution to the Vineyard method was formulated by Rice in 1985.[54–56] Further historical developments include various modifications to account for quantum effects during hydrogen diffusion.[57–60]

2.4 Equivalence of the Eyring and Vineyard theory

Many authors refer to the equivalence of the Eyring and the Vineyard method in the harmonic approximation at high temperature in case only phonons at the Gamma point are considered in both methods.[5,61,62] Indeed many groups calculate phonon modes for the Gamma point only[63–65] unless thermodynamic properties derived from the phonon dispersion on the whole reciprocal lattice grid are of special interest.[63,64,66–69] According to this, the vibrational free energy is sometimes calculated for several phonon wave vectors q (q-point mesh),[5,70–73] extending the Eyring method to the full Brillouin zone. In fact, also the Vineyard method can be applied to a phonon mesh with several wave vectors, but this possibility is only mentioned by Fedorov and Sadreev.[74] To our knowledge, there is no example in literature in which the equivalence of the Eyring and the Vineyard method is shown without restriction to the Gamma point. For this reason, we will describe this derivation in the following.

The canonical partition function for M discrete wave vectors

with the index q is defined as

$$
Z_{\mathrm{vib}} = \prod_{q}^{M} \left(\prod_{i}^{N} \sum_{n} e^{-\frac{E_{q,i,n}}{k_{\mathrm{B}}T}} \right)^{\frac{1}{M}},
\tag{16}
$$

where the N phonon bands, equivalent to the degrees of freedom, have the index i and the microstates have the index n.¶ For the vibrational partition function, the harmonic approximation and therewith the energy eigenvalues $E_{q,i,n} = hv_{q,i}(1/2+n)$ of the quantum harmonic oscillator with its frequency $v_{q,i}$ can be used (see also Maradudin[75] and Wimmer *et al.*[62]). The vibrational energy F_{vib} can be calculated from the partition function $F_{\mathrm{vib}} = -k_{\mathrm{B}}T \ln Z_{\mathrm{vib}}$ resulting in

$$
\begin{aligned}
F_{\mathrm{vib}} &= \sum_{q,i} \left\{ \frac{hv_{q,i}}{2M} + \frac{k_{\mathrm{B}}T}{M} \ln \left[1 - \exp \left(\frac{-hv_{q,i}}{k_{\mathrm{B}}T} \right) \right] \right\} \\
&= \frac{k_{\mathrm{B}}T}{M} \sum_{q,i} \ln \left(2 \sinh \frac{hv_{q,i}}{2k_{\mathrm{B}}T} \right).
\end{aligned}
\tag{17}
$$

Here $\sum_{q,i} hv_{q,i}/2M$ is independent of temperature and can be regarded as zero point energy correction to the energy barrier ΔE_{el}^0. The attempt frequency can be calculated corresponding to the Eyring theory (Eq. 8):

$$
\begin{aligned}
v_0 &= \frac{k_{\mathrm{B}}T}{h} \frac{\prod\limits_{q}^{M} \prod\limits_{i}^{N} \left(2 \sinh \frac{hv_{q,i}}{2k_{\mathrm{B}}T} \right)^{\frac{1}{M}}}{\prod\limits_{m}^{M} \prod\limits_{j}^{N-1} \left(2 \sinh \frac{hv_{m,j}}{2k_{\mathrm{B}}T} \right)^{\frac{1}{M}}} \\
&\approx \frac{k_{\mathrm{B}}T}{h} \frac{\prod\limits_{q}^{M} \prod\limits_{i}^{N} \left(1 - e^{-\frac{hv_{q,i}}{k_{\mathrm{B}}T}} \right)^{\frac{1}{M}}}{\prod\limits_{m}^{M} \prod\limits_{j}^{N-1} \left(1 - e^{-\frac{hv_{m,j}}{k_{\mathrm{B}}T}} \right)^{\frac{1}{M}}}.
\end{aligned}
\tag{18}
$$

The indices i (phonon band) and q (wave vector) for the initial state correspond to the indices j and m for the transition state. The transition state has one degree of freedom less than the initial state. For the last part in Eq. 18, which is given for comparison with literature, it is assumed that the difference in zero point energy can be neglected, which might be valid at high temperature.[76]

As a further approach that is often performed in literature, the Taylor expansion of the hyperbolic sine can be simplified for high temperatures (see Eq. 19) to $\sinh x \approx x$. Equation 19 is often referred to as the classical limit[77] of the vibrational free energy of the 'quantum mechanical' vibrational free energy in Eq. 17.

$$
F_{\mathrm{vib}} = \frac{k_{\mathrm{B}}T}{M} \sum_{q,i} \ln \left(\frac{hv_{q,i}}{k_{\mathrm{B}}T} \right)
\tag{19}
$$

¶ The partition function is calculated as geometric mean for all discrete wave vectors, just as the arithmetic mean of all wave vectors would be used for the phonon density of states to satisfy its normalization condition.

This journal is © the Owner Societies 2017

Phys. Chem. Chem. Phys., 2017, **19**, 9957 | 1–17 | 5

Inserting Eq. 19 in the Eyring formula (Eq. 8) leads to

$$\nu_0 = \frac{\prod\limits_{q}^{M}\prod\limits_{i}^{N} \nu_{q,i}^{\frac{1}{M}}}{\prod\limits_{m}^{M}\prod\limits_{j}^{N-1} \nu_{m,j}^{\frac{1}{M}}}. \qquad (20)$$

The resulting attempt frequency (Eq. 20) allows the general use of the classical Vineyard method for high temperatures and any phonon mesh. If only the Gamma point is considered ($M = 1$), the classical Vineyard formula (Eq. 15) is obtained.

3   Computational details

All calculations were performed by means of density functional theory within the generalized gradient approximation (GGA) according to Perdew, Burke and Ernzerhof[78] (PBE) and the projector augmented-wave method[79] (PAW) using the Vienna Ab initio Simulation Package (VASP).[80,81] Plane waves with an energy cutoff of 500 eV and a $2 \times 2 \times 2$ Monkhorst-Pack k-point mesh for the simulation cell constructed from 16 unit cells were applied according to an earlier publication.[17] The convergence parameters for electronic and ionic relaxation were set to 10^{-8} eV and 10^{-4} eV/Å, respectively, to guarantee a sufficient accuracy of the calculated forces. The $5s^2 5p^6 6s^2 5d^1 4f^1$ electrons of the cerium atoms, the $5s^2 5p^6 6s^2 5d^1$ electrons of the samarium atoms and the $2s^2 2p^4$ electrons of the oxygen atoms were treated as valence electrons. A Hubbard U parameter was introduced to account for the localization of strongly correlated electrons by the rotational invariant approach.[82] A value of 5 eV for the 4f-orbitals of cerium was chosen according to earlier studies.[17,20,26,83,84] For all defective cells, the total number of electrons in the cell was adapted to reproduce the actual charge state of the different defects, e.g. $(Ce_{64}O_{127})^{2+}$ for a simulation cell containing one oxygen vacancy.

The nudged elastic band method[85,86] (NEB) was applied to investigate the transition states and the minimum energy pathways. One ionic configuration for the saddle point configuration ('image') was interpolated from the initial and final state of the migration process. Tests with more than one intermediate image between the initial and final configuration of the migration showed no differences in the migration energies. The same is true for tests using the climbing image nudged elastic band method[87] (CI-NEB). The internal atomic positions in the cell were relaxed without changing the lattice parameter.

The phonon frequencies at constant volume were calculated using the finite difference method introduced by Parlinski et al.[88] with the commercial software MedeA. All investigated structures were relaxed according to the parameters given above. Starting from these structures, cells with atomic displacements of ± 0.005 Å were created automatically. For all created cells the electronic ground state was calculated and the Hellmann-Feynman forces acting on the ions were used to build the force constant matrix. After Fourier transformation, the diagonalization of the dynamical matrix yielded the phonon frequencies at different q-points. No longitudinal/transverse optical splitting (LO/TO) was applied according to Grieshammer et al.[17]
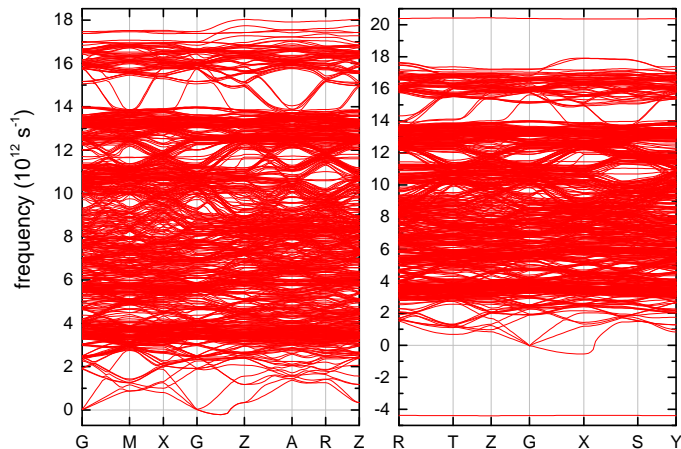

Fig. 3 Phonon dispersions of the initial state $V_{O1}^{\bullet\bullet} - O_{O2}^{\times}$ (left, space group $P\bar{4}m2$) and the transition state $V_{O1}^{\bullet\bullet} - O_{TS}^{''} - V_{O2}^{\bullet\bullet}$ (right, space group $Pmmm$) in ceria according to Eq. 7.

4   Results and discussion

Phonon dispersions for the initial and the transition state of the migration (see Eq. 7) showed minor contributions of imaginary frequencies at some q-points in the vicinity of the Gamma point that had to be taken into account (see Fig. 3, imaginary frequencies are shown as negative frequencies). The number of imaginary acoustic branches varies between initial and transition state. For this reason, occurring imaginary parts were disregarded symmetrically in initial and transition state as the resulting error is assumed to be small. In general, imaginary frequencies suggest an unstable structure leading to deformations along the associated phonon wave vectors. However, for some q-point samplings the occurring imaginary frequencies may be caused by non-cubic supercells, or, as shown by Grabowski et al.,[69,89] not fully converged parameters. The latter can probably be neglected since the results by Grabowski et al. suggest that our k-point mesh and supercell size are converged.[69,90] Furthermore, the supercell volume was doubled compared to previous phonon calculations.[17]

Figure 4 shows the vibrational free energy difference ΔF_{vib} and its components, the vibrational energy difference ΔE_{vib} and entropy difference of initial and transition state ΔS_{vib}, according to Eq. 9 in ceria in harmonic approximation for a $6 \times 6 \times 6$ phonon mesh. As previously mentioned, the vibrational energy difference is similar to $-k_B T$ as it differs less than 5% for temperatures above 900 K.

4.1   Pure ceria: Influence of the phonon mesh

The attempt frequency was calculated using the Eyring method[31] (Eq. 8) with Eq. 17 and our generalized Vineyard[32] method (Eq. 20) with different q-point mesh sizes. The attempt frequency rises to a plateau with increasing temperature (Fig. 5). Above 600 K both the Eyring and the generalized Vineyard method lead to similar attempt frequencies as predicted by theory. At 0 K the free vibrational energy difference between initial and transition state is 0.007 eV. Some authors move this zero point energy contribution of the attempt frequency (ZPE) to the migration energy
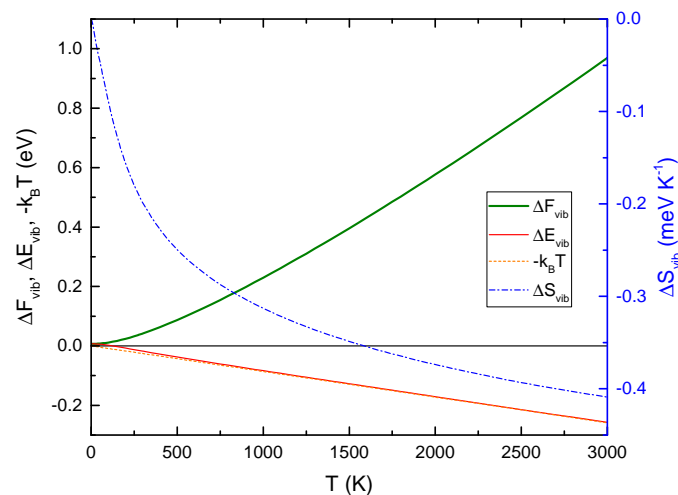
Fig. 4 Vibrational free energy difference ΔF_{vib}, vibrational energy difference ΔE_{vib} and entropy difference ΔS_{vib} of initial and transition state in ceria in harmonic approximation for a $6 \times 6 \times 6$ phonon mesh. For comparison $-k_B T$ is shown which is similar to ΔE_{vib}.

Fig. 5 Oxygen vacancy attempt frequency ν_0 in ceria in harmonic approximation for different phonon mesh sizes. Lines are calculated using the Eyring method, squares are the results of the generalized Vineyard formula. The dashed line shows the result according to the Eyring method without zero point energy (ZPE).

Table 1 Electronic migration energies for different migration configurations, distances of the edge cations in the initial and the transition state and oxygen vacancy attempt frequencies $\nu_0(V,T)$ (Vineyard) at constant volume ($V =$ const.)

migration edge	d_{IS} (Å)	d_{TS} (Å)	$d_{TS} - d_{IS}$ (Å)	$\Delta E_{el}^0(V,T)$ (eV)	$\nu_0(V,T)$ (s^{-1})
Ce-Ce	4.148	4.267	0.119	0.587	$1.47 \cdot 10^{12}$
Ce-Sm	4.142	4.268	0.126	0.759	$1.49 \cdot 10^{12}$
Sm-Sm	4.141	4.280	0.139	1.166	$4.30 \cdot 10^{12}$

leading to another definition of the attempt frequency, which is larger especially at low temperatures.[5,76,91,92] For the calculation of the phonon dispersion, an equidistantly spaced q-point mesh of dimensions between $1 \times 1 \times 1$ and $6 \times 6 \times 6$ was applied to sample the phonon dispersion, since the number of all possible discrete wave vectors is too large (Eq. 16). It can be clearly seen that the common reduction to the Gamma point ($1 \times 1 \times 1$) is not sufficient to calculate the attempt frequency. The convergence of the phonon mesh is reached only above 64 q-points corresponding to a $4 \times 4 \times 4$ grid. The resulting attempt frequency in pure ceria $1.5 \cdot 10^{12}$ s^{-1} is in the range of the usually assumed values ($10^{12} - 10^{13}$ s^{-1}).

4.2 Sm doped ceria

The influence of doping with Sm on the attempt frequency was investigated. Therefore, one or two samarium dopants were introduced at the migration edge (see Fig. 1) between two edge-sharing tetrahedra. A convergence of the resulting attempt frequencies as a function of the used phonon mesh was observed, similar to pure ceria, while the approximation of the attempt frequency based on Gamma point calculations was even worse. All further results correspond to the $6 \times 6 \times 6$ phonon mesh. Surprisingly one samarium dopant does not influence the attempt frequency whereas two samarium dopants increase the attempt frequency by a factor of three (Table 1). The increase in attempt frequency for the Sm-Sm edge compared to pure ceria is expected due to the higher activation barrier and steeper electronic energy curvature. For the Ce-Sm edge, the migrating oxygen ion deviates from the direct, straight path found for the Ce-Ce and the Sm-Sm edge between initial and final position. The migrating oxygen ion follows a curved path by avoiding the steeper electronic energy curvature and a high attempt frequency. Surprisingly, this leads to similar attempt frequencies for one Sm dopant and pure ceria. The resulting attempt frequencies for the Ce-Ce and Ce-Sm edge are in agreement with literature in which a constant attempt
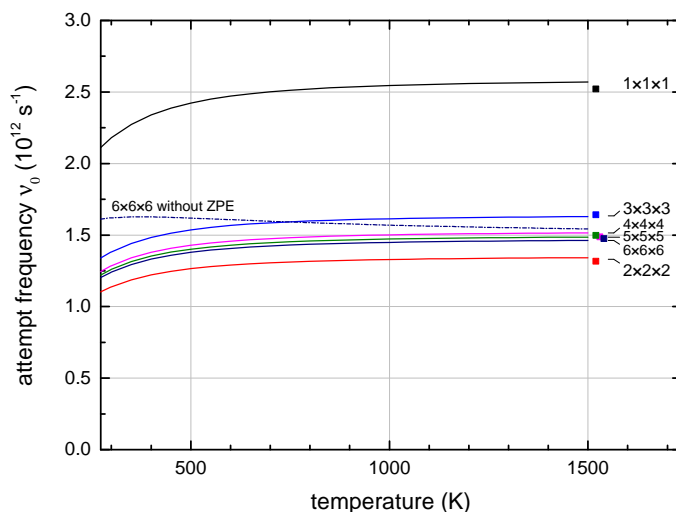
frequency for different configurations is either assumed[18] or calculated for both the Ce-Ce and Ce-Gd edge.[10] Here, Tarancón *et al.* did not consider the Gd-Gd edge due to "the negligible impact on the final diffusion properties".

A key property for the interaction between the edge cations and the migrating oxygen ion are the distances of the edge cations in the transition state d_{TS} and the initial state d_{IS} (see Table 1). The migration energies ΔE_{el}^0 of the different edge configurations depend linearly on the difference of the distances of the edge cations between transition and initial state, $d_{TS} - d_{IS}$. Simply described, the cations at the edge must be pushed apart during an oxygen ion jump. This leads to a linear relationship between the widening of the edge cations and the migration energy. Likewise, the attempt frequency is majorly influenced by the edge cation distance in the transition state d_{TS}. For the Ce-Ce and Ce-Sm edge ν_0 and d_{TS} are similar, respectively. Both values increase significantly for the Sm-Sm edge.

For further investigation and in consideration of the very time-consuming phonon calculations, the attempt frequency could be described in a simple approximation by displacing the migrating oxygen ion in the initial state. Using the classical harmonic oscillator with the displacement x and the electronic energy $E_{el}^0 = \frac{1}{2}kx^2 + E_{el,x=0}^0$ the attempt frequency can be calculated according to $\nu_0 = \frac{\sqrt{k/m}}{2\pi}$ with the mass m of the migrating oxygen ion.

This journal is © the Owner Societies 2017

Phys. Chem. Chem. Phys., 2017, **19**, 9957 | 1–17 | 7

In this simplified case, it is assumed that all neighboring atoms are frozen similar to the Einstein model (one body problem), a classical model can be used and only the initial state has an influence on the attempt frequency. This simple static displacement model leads to similar attempt frequencies for all three edge configurations (Fig. 1) with a slight increase for more Sm dopants from $8.42 \cdot 10^{12}$ to $9.74 \cdot 10^{12}$ s^{-1} (see Fig. 6). Analogous bulk calculations without any oxygen vacancy lead to a frequency of $11 \cdot 10^{12}$ s^{-1}. The attempt frequencies according to the static displacement model are higher than the values from the phonon calculations indicating a hard potential around the initial state. As described, the phonon calculations revealed an exceptionally high attempt frequency for the Sm-Sm edge. This deviation from the static displacement result indicates a strong influence of the neighboring atoms for the Sm-Sm edge as established above.

4.3 Attempt frequency at constant pressure in quasi-harmonic approximation

All phonon calculations were performed isochoric, i.e. for a constant volume that was derived for bulk ceria at the absolute zero. This follows the harmonic approximation in which all calculations are performed at a fixed equilibrium volume. To investigate the isobaric behavior, i.e. the constant pressure case ($p = 0$), the quasi-harmonic approximation can be applied in which the minimum of the free energy for different volumes is determined at given temperatures. Therefore, all properties like the migration energy should be calculated at constant pressure (Eq. 13). The influence of the change between constant volume and constant pressure case on the electronic migration energy at zero temperature ΔE_{el}^0 is small (± 0.015 eV), and the exponential factor varies below $\pm 20\%$ at 900 K (compare Table 1 and 2). As phonon calculations are computationally demanding it is commonly assumed that the change in vibrational entropy with changing volume, $\left(\frac{\partial S_{vib}}{\partial V} \right)_T$, is similar in defect-free bulk, the defective cell in the initial state and in the transition state.[93,94] Starting from the equilibrium volume V_0, the entropy of migration for $p = 0$ is given according to Grieshammer et al.[17]

$$\Delta S_{vib}(p, T) = \Delta S_{vib}(V(p, T), T)$$

$$= \Delta S_{vib}(V_0, T) + \int_{V_{IS}(p,T)}^{V_{IS}(p,T)+\Delta V} \left(\frac{\partial S_{vib}}{\partial V} \right)_T^{bulk} dV$$

$$= \Delta S_{vib}(V_0, T) + \alpha_V B_T \cdot \Delta V, \tag{21}$$

with the change in volume between transition state and initial state at constant pressure $\Delta V = V_{TS}(p = 0, T) - V_{IS}(p = 0, T)$ which is assumed to be independent of temperature. Alternatively, the change in pressure between transition state and initial state at constant volume Δp can be used (see Eq. 22). The volumetric thermal expansion coefficient α_V and the bulk modulus B_T for bulk ceria were already determined by Grieshammer et al.[17] The free vibrational energy of migration ΔF_{vib} is defined by the vibrational energy ΔE_{vib} and entropy ΔS_{vib} (see Eq. 9). The free vibrational energy of migration at zero pressure can then be writ-

Table 2 Electronic migration energies for different migration configurations, changes in volume between transition state and initial state ΔV and oxygen vacancy attempt frequencies $v_0(p, T)$ (Vineyard) at constant pressure ($p = 0$) and 900 K

migration edge	$\Delta E_{el}^0(p,T)$ (eV)	ΔV (Å^3)	$v_0(p,T)$ (s^{-1})
Ce-Ce	0.602	3.06	$7.67 \cdot 10^{12}$
Ce-Sm	0.769	3.01	$7.52 \cdot 10^{12}$
Sm-Sm	1.162	2.64	$1.79 \cdot 10^{13}$

ten as

$$\Delta F_{vib}(p, T) = \Delta F_{vib}(V_0, T) - T \cdot \alpha_V B_T \cdot \Delta V$$

$$= \Delta F_{vib}(V_0, T) + T \cdot \alpha_V V \cdot \Delta p. \tag{22}$$

Therewith the generalized Vineyard result (Eq. 20) can be modified:[95]

$$v_0(p) = \frac{\prod_{q,i} v_{q,i}^{\frac{1}{M}}}{\prod_{m,j} v_{m,j}^{\frac{1}{M}}} \exp\left(\frac{\alpha_V B_T \Delta V}{k_B} \right). \tag{23}$$

The same modification applies to the Eyring formula (Eq. 8):

$$v_0(p, T) = \frac{k_B T}{h} \exp\left(\frac{-\Delta F_{vib}(V_0, T)}{k_B T} \right)$$

$$\times \exp\left(\frac{\alpha_V B_T \Delta V}{k_B} \right). \tag{24}$$

In Fig. 6 and 7, the attempt frequencies in samarium doped ceria for the relaxed cell volume ($p = 0$) are shown. We can now compare the constant volume with the constant pressure case: The hydrostatic pressure for the constant volume case (V_0) results in a volume compression for the Ce-Ce, Ce-Sm edge and an expansion for the Sm-Sm edge for the constant pressure case for both initial state [$V_{IS}(p, T)$] and transition state [$V_{TS}(p, T)$]. In the constant pressure case, the change in volume between transition state and initial state ΔV is similar for the Ce-Ce and Ce-Sm edge and slightly smaller for the Sm-Sm edge (see Table 2). The influence of $\alpha_V B_T \Delta V$ in Eq. 21 on the attempt frequency is significant. Minor errors in $\alpha_V B_T$ are propagated exponentially in the attempt frequency as shown in Fig. 6 and 7. Thus, the error of the attempt frequency is larger than 10% above 1500 K. The attempt frequency at constant pressure increases compared to the constant volume case by a factor of about five for the Ce-Ce and Ce-Sm edge and four for the Sm-Sm edge at 900 K. The resulting attempt frequencies are roughly in the range of the usually assumed values ($10^{12} - 10^{13}$ s^{-1}) and similar to experimental Debye frequencies in ceria which are between $8 \cdot 10^{12}$ and $10 \cdot 10^{12}$ s^{-1} according to ultrasonic pulse, specific heat and thermal expansion coefficient measurements.[96–99]

4.4 Experimental values for pure ceria

Although the Vineyard method directly uses the normal mode frequencies in the initial and transition state, their resulting ratio defines a frequency that differs from any existing frequency
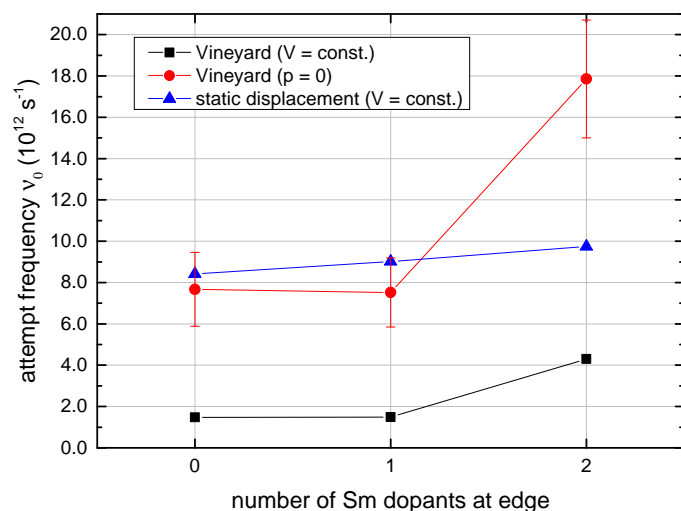
Fig. 6 Oxygen vacancy attempt frequency ν_0 in harmonic (squares) and quasi-harmonic approximation (circles) in samarium doped ceria with different number of dopants at the migration edge, using the generalized Vineyard method at a temperature of 900 K. For comparison also the results of the simple displacement approximation (triangles) are shown.

Fig. 7 Oxygen vacancy attempt frequency ν_0 in pure ceria in harmonic and quasi-harmonic approximation calculated using the Eyring (lines) and generalized Vineyard (squares) method at a temperature of 900 K at constant volume ($V = $ const.) and constant pressure ($p = 0$).

in the real lattice.[34] However, the attempt frequency of oxygen ion jumps can be extracted as an average macroscopic property based on the temperature dependence of the oxygen ion conductivity or the oxygen diffusion coefficient. Common experiments to examine the experimental attempt frequency are therefore direct current measurements (DC), impedance spectroscopy (AC), secondary ion mass spectrometry (SIMS) and gas phase analysis (GPA). Experimental attempt frequencies and oxygen vacancy diffusion coefficients are shown in Table 3 and Fig. 8. Error bars are calculated based on the scattering of the diffusion coefficient.

SIMS and GPA experiments were used by Floyd[101] and Kamiya *et al.*[103,104] to investigate the oxygen tracer diffusion coefficient $D^*_{O^{2-}}$. The oxygen tracer diffusion coefficient is related to the oxygen self-diffusion coefficient $D_{O^{2-}}$ by a correlation factor $f_{O^{2-}}$ according to $D^*_{O^{2-}} = f_{O^{2-}} D_{O^{2-}}$. In contrast to the jumps of an oxygen vacancy, the jumps of a tracer ion are correlated, leading to a smaller mean square displacement for the tracer and a correlation factor below unity. For vacancy diffusion in a simple cubic lattice the correlation factor is 0.65 at very low defect concentrations. Beyond that, the tracer correlation factor is a function of the defect concentration: Increasing vacancy concentrations decrease the probability of 'return jumps' for a tracer atom, the tracer correlation decreases and $f_{O^{2-}}$ increases. In addition, for increasing defect concentration the ion-vacancy interaction increases and the distribution of conducting ions influences the tracer correlation factor.[3] Therefore, the here used correlation factor ($f_{O^{2-}} = 0.65$) is an approximation.

The oxygen self-diffusion coefficient $D_{O^{2-}}$ is related to the oxygen vacancy self-diffusion coefficient $D_{V_O^{\bullet\bullet}}$ according to Eq. 3 using the charge carrier concentration. For pure ceria at oxidizing conditions, the determination of the concentration is quite difficult as oxygen vacancies exist due to (extrinsic) impurities, reduction and intrinsic disorder. However, many studies point out a high impurity concentration compared to the intrinsic- (anti-
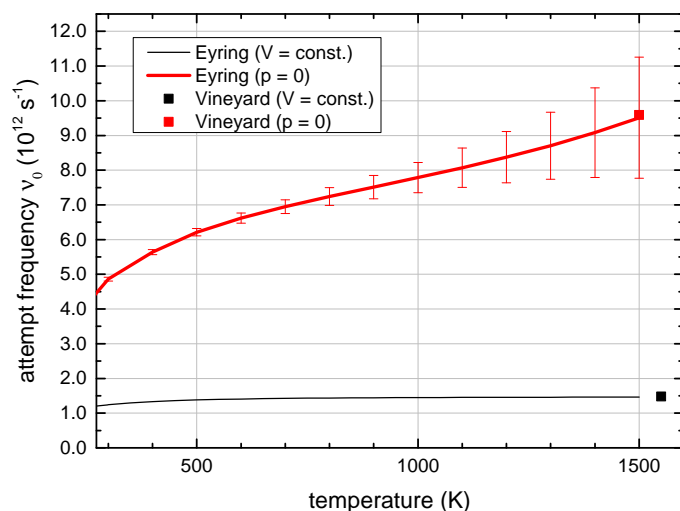
Frenkel) or reduction-dominated oxygen vacancy concentration at $p(O_2) = 0.2$ bar for temperatures below 800 °C.[17,26,106,107] At higher temperatures, the oxygen vacancy concentration increases especially due to reduction, though it could only be roughly estimated for experimental samples with unknown impurities. Therefore, in this work, the charge carrier concentration for all temperatures was derived from the purity of the starting materials according to literature assuming trivalent impurities[100,101,103,104] or, for one sample, from mass spectrographic analysis.[102,108] The error of the charge carrier concentration is estimated to be well below one order of magnitude. The approximated oxygen vacancy concentration varies over two orders of magnitude for stoichiometric ceria ($10^{17} – 10^{19}$ cm^{-3}) and is a reason for scattering of the extracted oxygen vacancy self-diffusion coefficient [see Fig. 8(a)].

In literature, direct current measurements and impedance spectroscopy experiments were used to measure the oxygen ion conductivity.[21,100,102,105] In this work, additional impedance spectroscopy experiments were performed (see Appendix). Using the charge carrier concentration, the conductivity can be converted into the 'conductivity' diffusion coefficient or charge diffusion coefficient of the oxygen ions $D_{\sigma,O^{2-}}$, which is defined according to the classical Nernst-Einstein equation (Eq. 1). It should be noted that $D_{\sigma,O^{2-}}$ has the dimensions of a diffusion coefficient but is not defined by Fick's first law. Conductivity and tracer diffusion coefficients can be compared using the Haven Ratio $H_R = D^*_{O^{2-}}/D_{\sigma,O^{2-}}$.[3,109] Only for non-interacting defects the Haven Ratio is equal to the tracer correlation factor. Otherwise, a thermodynamic factor has to be considered, which was neglected in this work. Based on this assumption, the conductivity diffusion coefficient $D_{\sigma,O^{2-}}$ can be converted in the oxygen vacancy self-diffusion coefficient $D_{V_O^{\bullet\bullet}}$ according to Eq. 3 using again the charge carrier concentration.

Experimental attempt frequencies $\overline{\nu}_{\exp,V_O^{\bullet\bullet}}$ and activation enthalpies ΔH_a can be extracted as an average macroscopic property

Table 3 Experimental oxygen vacancy attempt frequency $\bar{v}_{\mathrm{exp},V_O^{\bullet\bullet}}$ of pure ceria for polycrystalline samples (poly) and single crystals (sc) calculated based on impedance spectroscopy (AC), direct current (DC), secondary ion mass spectrometry (SIMS) and gas phase analysis (GPA) measurements. The number of charge carriers is based on the purity (hp = high, lp = low) of the starting material or the non-stoichiometry for [a] $CeO_{1.992}$ and [b] $CeO_{1.96}$. The error of the attempt frequency is given according to the linear regression.

source	crystallinity	method	domain	T (°C)	$\bar{v}_{\mathrm{exp},V_O^{\bullet\bullet}}$ (s^{-1})
this work	poly	AC	bulk	227−733	$(9 \pm 2) \cdot 10^{14}$
Wang et al. [100]	poly[hp]	AC	bulk	237−352	$(9 \pm 4) \cdot 10^{13}$
Wang et al. [100]	poly[lp]	AC	bulk	237−596	$(8 \pm 1) \cdot 10^{13}$
Floyd [101]	sc	GPA	bulk	836−1151	$(2 \pm 3) \cdot 10^{15}$
Brugner et al. [102]	sc, poly	DC	bulk, total	1200−1500	$(6.7 \pm 0.8) \cdot 10^{19}$
Wang et al. [100]	poly[hp]	AC, DC	total	621−847	$5.2 \cdot 10^{21}$
Wang et al. [100]	poly[lp]	AC, DC	total	507−891	$4.9 \cdot 10^{17}$
Kamiya et al. [103]	poly	SIMS	total	1095−1297	$(1.6 \pm 0.9) \cdot 10^{20}$
Kamiya et al. [103]	poly	SIMS	total	797−895	$(3 \pm 5) \cdot 10^{14}$
Kamiya et al. [104]	poly	GPA	total	1094−1296	$(3 \pm 2) \cdot 10^{22}$
Tuller et al. [21]	sc[a]	AC, DC	bulk	200−1150	$2.3 \cdot 10^{13}$
Naik et al. [105]	poly[b]	DC	total	1030−1330	$(1.1 \pm 0.2) \cdot 10^{13}$

from the Arrhenius behavior of the oxygen vacancy self-diffusion coefficient $D_{V_O^{\bullet\bullet}}$ according to Eq. 2 for a known jump distance and geometrical factor (Eq. 1). Surprisingly, the experimental attempt frequency for pure ceria varies vastly between $10^{13} - 10^{22}$ s^{-1} (Table 3). In the following section, we will explain that all experiments are probably based on the same elemental frequency for a jump process.

4.5 Reasons for scattering of the experimental attempt frequency

The vast scattering of the experimental attempt frequency is caused by measurement technique, sample properties and temperature range.

Minor influences of the *measurement technique* include measuring inaccuracies, different experimental methods for either tracer diffusion or conductivity and the conversion of $D_{O^{2-}}^*$ and $D_{\sigma,O^{2-}}$ to the oxygen vacancy self-diffusion coefficient. Measuring inaccuracies are assumed to be small, especially since the experimental attempt frequency is extrapolated from measurements at several temperatures. Oxygen tracer diffusion coefficients and conductivities from different experiments differ due to diverse oxygen vacancy concentrations: The oxygen tracer diffusion coefficients of SIMS and GPA measurements for pure ceria vary about one order of magnitude. [101,103,104] The ionic conductivities measured in the present work and literature vary up to two orders of magnitude. [100,102,105] However, similar results for one sample are expected using different experimental methods. For example, Tuller et al. [21] observed the same ionic conductivity for single crystals using impedance spectroscopy and direct current measurements. To compare the different experiments the charge carrier concentration has to be approximated, which is a reason for scattering of the oxygen vacancy self-diffusion coefficient. Furthermore, $D_{O^{2-}}^*$ and $D_{\sigma,O^{2-}}$ are compared, thereby approximating values for the tracer correlation factor and the thermodynamic factor. For Gd doped ceria single crystals, where the charge carrier concentration is well defined, Ruiz-Trejo et al. [110] reported a tracer diffusion coefficient based on SIMS measurements one order of magnitude smaller than the conductivity diffusion coefficient. Here, the Haven Ratio is one order of magnitude smaller due to the

thermodynamic factor. In the related fluorite structure, 9.5 mol% single crystal yttria-stabilized zirconia (YSZ), Manning et al. [111] reported a Haven Ratio of 0.33 for low and 0.48 for high temperature. Both examples give a lower product of tracer correlation factor and thermodynamic factor than assumed in this work, though this is expected for high defect concentrations. In this case, the Haven Ratio changes by a factor smaller than two due to the thermodynamic factor. For small defects concentrations as in pure ceria, the tracer correlation factor of 0.65 may be a good choice. Therefore, the conversion of $D_{O^{2-}}^*$ and $D_{\sigma,O^{2-}}$ to the oxygen vacancy self-diffusion coefficient has probably only a minor impact on the scattering of the experimental attempt frequency.

To validate the different macroscopic experimental techniques, the diffusion coefficients can be compared to microscopic nuclear magnetic resonance (NMR) measurements. Avila-Paredes et al. [112,113] measured the oxygen transport in $Ce_{0.95}Sc_{0.05}O_{1.975}$ using the bulk conductivity relaxation frequency from impedance spectroscopy measurements as well as the temperature dependence of ^{45}Sc magic-angle-spinning NMR line shapes. The resulting prefactors from the extrapolation of the oxygen vacancy hopping frequencies are similar for both impedance with $(4.6 \pm 0.1) \cdot 10^{13}$ s^{-1} and NMR measurements with $(4.3 \pm 1.1) \cdot 10^{13}$ s^{-1}. Fuda et al. [114] examined lightly Y doped ceria (0.02 – 0.6 mol% Y_2O_3) using NMR. They found the correlation times of the vacancy motion to be essentially independent of dopant fraction. The resulting prefactor from the extrapolation of the oxygen vacancy hopping frequency is $(2.8 \pm 0.3) \cdot 10^{12}$ s^{-1}. The nanocrystalline samples that are examined by Fuda et al. [114] feature a large grain boundary effect, while NMR measurements can give bulk properties for polycrystalline samples due to the low grain boundary volume as in the case of Avila-Paredes et al. [112,113] Both NMR results fit well with the calculated attempt frequencies for pure ceria.

A major influence on the macroscopic experimental attempt frequency are *sample properties* which include the mentioned diverse oxygen vacancy concentrations, the macroscopic structure composed of bulk and grain boundaries and different impurities. In this work, all calculations were performed in the bulk domain. In order to allow a better comparison of the calculated at-
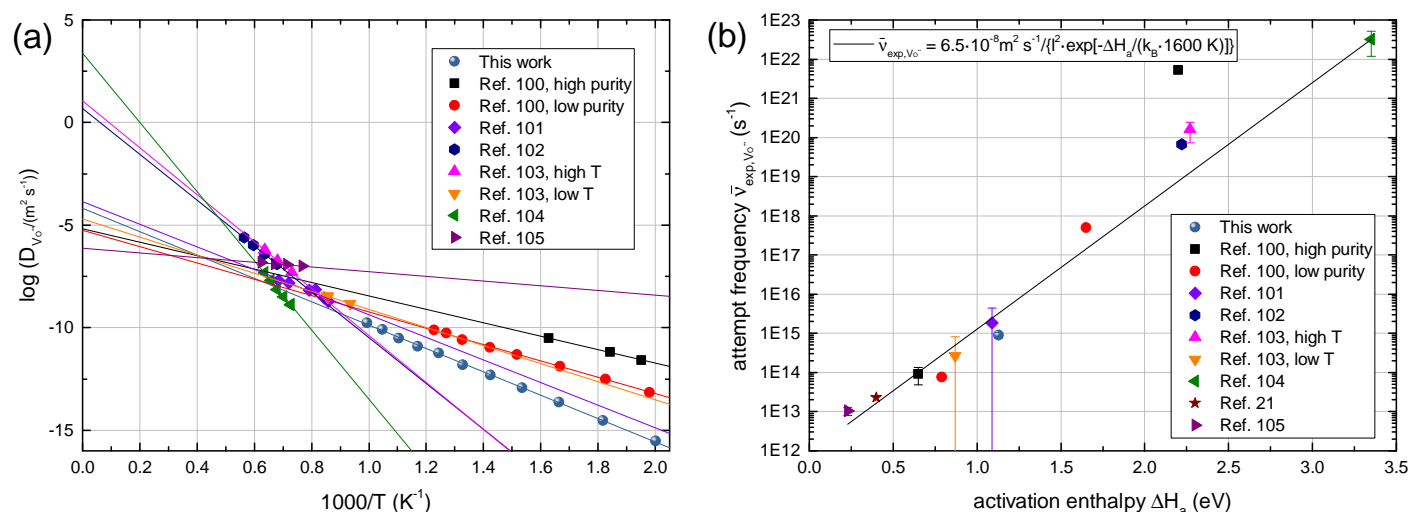
Fig. 8 Experimental (a) oxygen vacancy diffusion coefficients and (b) resulting attempt frequencies of pure ceria using bulk[100] and total[21,101–105] domain. Though experimental attempt frequencies vary over several orders of magnitude, all experiments are probably based on the same elemental frequency for a jump process.

tempt frequency with experimental values, single crystals should be used or bulk properties from polycrystalline samples should be extracted. Otherwise, the total conductivity or diffusion could result from the contribution of the bulk (grain, lattice) and the grain boundary domain. Impedance spectroscopy is an important tool to separate both contributions and has been extensively used on pure[21,100] and samarium doped ceria.[115–120] However, only a few authors specify the bulk ionic conductivity separately. Well known is the relation between bulk and grain boundary conductivity for rare-earth doped ceria: Zhan *et al.*[118] and Bellino *et al.*[115] separated the bulk, grain boundary and total conductivity of Sm and Y doped ceria showing a bulk conductivity that is larger than both grain boundary and total conductivity. The resulting experimental attempt frequency for the bulk is however only a fraction (0.8–0.005) compared to the experimental attempt frequency of the total domain caused by higher activation enthalpies for the total domain. For pure ceria, Wang *et al.*[100] measured bulk conductivities orders of magnitude larger than the total conductivity with an activation enthalpy lower than for the total domain. In fact, Figure 8 and Table 3 show, for most stoichiometric ceria measurements, higher ΔH_a and higher $\bar{v}_{\mathrm{exp},V_O^{\bullet\bullet}}$ for the total domain compared to the bulk. While the experimental attempt frequencies for the bulk domain fit well with the calculated attempt frequencies for pure ceria, the attempt frequencies for the total domain are significantly higher. However, Brugner *et al.*[102] reported the same conductivity for polycrystalline samples and single crystals resulting in the same experimental attempt frequency though compared to other bulk measurements $\bar{v}_{\mathrm{exp},V_O^{\bullet\bullet}}$ is very large here. Furthermore, it has been shown that the contribution from the grain boundaries to the total resistivity diminishes at high temperature.[121] Therefore, also attempt frequencies for the total domain are shown included in Fig. 8.

Beyond the macroscopic structure, even small amounts of impurities that associate with oxygen vacancies, e.g. small rare-earth cations, can increase the activation enthalpy. While the

impact on the oxygen vacancy self-diffusion coefficient at intermediate temperatures might be small, different impurities may lead to different activation enthalpies, which would significantly influence the experimental attempt frequency. Therefore, we performed kinetic Monte Carlo simulations similarly to an earlier work[20] between 500 and 800 °C without considering changes in the jump attempt frequency or the existence of polarons. For all jumps the calculated jump attempt frequency ($1.47 \cdot 10^{12}$ s^{-1}) was applied and in pure ceria a migration energy of 0.47 eV was used. Subsequently, the conductivity was fitted according to Eq. 2. In contrast to CeO$_{1.99995}$, where ΔH_a and $\bar{v}_{\mathrm{exp},V_O^{\bullet\bullet}}$ are similar to the input values, for Ce$_{0.999}$Sc$_{0.001}$O$_{1.9995}$ the apparent activation enthalpy (1 eV) and attempt frequency ($1.54 \cdot 10^{14}$ s^{-1}) increase significantly, while the oxygen vacancy self-diffusion coefficient decreases up to two orders of magnitude. This effect can only be observed for dopants with strong association between dopant and oxygen vacancy. For lightly Sm or La doped ceria, no significant influence on oxygen vacancy self-diffusion coefficient, activation enthalpy and attempt frequency can be observed. Therefore, different impurities can significantly influence the experimental attempt frequency. Experimentally, this can be seen e.g. in the conductivity measurements by Wang *et al.*[100]

Finally, the macroscopic experimental attempt frequency is influenced by the measured *temperature range* due to the above-discussed influences. While the conductivity and the oxygen tracer diffusion coefficient are continuous with temperature, the activation enthalpy may change for different temperature regimes. This leads to kinks in the oxygen vacancy self-diffusion coefficient and jumps in the experimental attempt frequency if a constant charge carrier concentration is assumed. Two types of kinks are well known in literature: For a change from a low-temperature region dominated by impurities to a high-temperature region dominated by reduction, the activation enthalpy increases abruptly for higher temperatures. As the number of oxygen vacancies created by reduction (or intrinsic dis-

This journal is © the Owner Societies 2017

Phys. Chem. Chem. Phys., 2017, **19**, 9957| 1–17 | 11

order) increases with temperature, their concentration may exceed the number of defects created by impurities. Defects created by reduction and intrinsic defects have to be formed leading to an increase in activation enthalpy.[1,103] Actually, Kamiya et al.[103] reported for low temperature an experimental attempt frequency orders of magnitude lower than for high temperature indicating a change from an impurity- to a reduction-dominated regime. It shall be mentioned that Kamiya et al. measured penetration depths for low temperature similar to the grain size of pure ceria, which might lead to bulk dominated properties while at high temperatures the penetration depths are orders of magnitude higher.[122] Therefore, the change in attempt frequency of six orders of magnitude results from both the change in bulk and grain boundary dominated regime as well as the defect chemistry transition. Ideally, for investigating reduction-dominated regions, the change in the charge carrier concentration should be included in the oxygen vacancy self-diffusion coefficient, which might lead to similar experimental attempt frequencies at both temperature regimes.

The second type of kink is a decrease in activation enthalpy for higher temperatures caused by a change in the diffusion behavior for different temperatures, especially for non-stoichiometric or doped ceria.[115,121,123–125] Zhan et al.[118] described a critical curvature temperature T_b for Sm doped ceria. Below this temperature, oxygen vacancies are trapped by samarium ions $\left[\mathrm{Sm}'_{\mathrm{Ce}} - \mathrm{V}_{\mathrm{O}}^{\bullet\bullet}\right]$. Therefore, ΔH_a is the sum of the 'migration enthalpy' of the oxygen ions and the association enthalpy of $\left[\mathrm{Sm}'_{\mathrm{Ce}} - \mathrm{V}_{\mathrm{O}}^{\bullet\bullet}\right]$ while at higher temperature ΔH_a is equivalent to the 'migration enthalpy' of the oxygen ions. This causes a kink in the ionic conductivity in the Arrhenius plot leading to lower activation enthalpies and prefactors at high temperatures. This kink can be reproduced using kinetic Monte Carlo simulation although further influences on the activation enthalpy are given.[20,126] For another perspective on this effect, Zhan et al. assume that the concentration of the oxygen vacancies depends on the association enthalpy of the forming $\left[\mathrm{Sm}'_{\mathrm{Ce}} - \mathrm{V}_{\mathrm{O}}^{\bullet\bullet}\right]$ defect complexes at low temperature while at $T > T_b$ the concentration of oxygen vacancies is set by the dopant fraction, as all oxygen vacancies are free. Taking into consideration that the association reduces the oxygen vacancy concentration, this could lead to the same attempt frequencies at low and high temperatures. Therefore, the experimental attempt frequency can only be extracted above the critical curvature temperature if the degree of association is unknown. We examined this effect using kinetic Monte Carlo simulations similar to an earlier work[20] without considering changes in the jump attempt frequency. Although Zhan et al. investigate highly doped ceria, the kinetic Monte Carlo simulations show this effect for Sc doped ceria for dopant fractions as low as $\mathrm{Ce}_{0.99998}\mathrm{Sc}_{0.00002}\mathrm{O}_{1.99999}$ around $T_b = 800$ °C. For the above-mentioned $\mathrm{Ce}_{0.999}\mathrm{Sc}_{0.001}\mathrm{O}_{1.9995}$, apparent activation enthalpy (0.67 eV) and attempt frequency ($4.65 \cdot 10^{12}$ s^{-1}) decrease again for conductivities fitted between 1100 and 1300 °C. Therefore, a change in the diffusion behavior can change the experimental attempt frequency by two orders of magnitude. However, impedance measurements of the bulk domain in pure ceria are commonly limited to low temperatures due to a restricted frequency range.

Obviously, measurements of non-stoichiometric ceria might lead to different results as the presence of polarons changes the diffusion behavior. In fact, the smallest activation enthalpies in this work are the ones measured by Tuller et al.[21] and Naik et al.[105] [see Fig. 8(b)].

In summary, differences in measurement technique, sample properties or investigated temperature range change the oxygen self-diffusion coefficient by about two orders of magnitude at intermediate temperature [see Fig. 8(a)]. The vast scattering of the experimental attempt frequency in the range of nine orders of magnitude is caused by a change in activation enthalpy. Especially different contributions of bulk and grain boundary domain to the total conductivity or diffusion, different impurities, a change from an impurity- to a reduction-dominated regime and a change in the diffusion behavior can lead to significant changes in the activation enthalpy. A closer examination shows a clear dependence of the experimental attempt frequency on the activation enthalpy [Fig. 8(b)]. As diffusion coefficients are extrapolated to infinite temperature to obtain experimental attempt frequencies, larger activation enthalpies lead obviously to larger attempt frequencies. If now the oxygen tracer diffusion coefficient is identical for all measurements at a specific temperature, the relation between experimental attempt frequency and activation enthalpy is given by

$$D_{\mathrm{V}_{\mathrm{O}}^{\bullet\bullet}} = l^2 \cdot \overline{v}_{\mathrm{exp},\mathrm{V}_{\mathrm{O}}^{\bullet\bullet}} \cdot \exp\left(-\frac{\Delta H_a}{k_B T}\right). \qquad (25)$$

All oxygen vacancy diffusion coefficients were fitted according to Arrhenius (Eq. 2). Using the resulting activation enthalpies and experimental attempt frequencies, an average oxygen vacancy diffusion coefficient at 1600 K was fitted (Eq. 25). Here, 1600 K showed the best agreement for all measurements. Figure 8(a) already shows that all $D_{\mathrm{V}_{\mathrm{O}}^{\bullet\bullet}}$ can be described as a function of $\overline{v}_{\mathrm{exp},\mathrm{V}_{\mathrm{O}}^{\bullet\bullet}}$ and ΔH_a using an average oxygen vacancy diffusion coefficient at 1600 K. This is even true for non-stoichiometric ceria. An exception is the measurement of Wang et al. of the total domain for the high purity sample, probably due to the large grain boundary contributions at low temperature measurements.[100] The good correlation of Eq. 25 in Fig. 8(b) is not surprising since it follows the classical rule $\Delta S = \frac{\Delta H}{T_c} + b$ with the constants T_c and b. A linear relationship between activation enthalpy and activation entropy has been found in physical, chemical and biological processes.[127,128] The enthalpy-entropy relation is in literature referred to as compensation rule or Meyer-Neldel rule.[129] The additional term 'isokinetic relation' refers to the common intersection point in an Arrhenius plot as shown in Fig. 8(a). Many investigations present an empirical relationship in experiments. However, e.g. Kemeny and Mahanti show that activation enthalpy and entropy are proportional to the number of vibrational degrees of freedom for electronic charge transport using a quadratic generalization of Holstein's one-dimensional linear polaron theory.[130] As the compensation rule applies to a series of closely related chemical reactions, we conclude that all presented measurements are linked and assume that a change in the activation enthalpy deter-

mines the experimental activation entropy. Therefore, it may be still possible that all experiments are based on the same elemental frequency for a jump process, which is similar to the calculated attempt frequency. Changes in the activation enthalpy are caused by grain boundary contributions for the total domain, measurements of reduction-dominated regions or the association of oxygen vacancies and impurities as recapitulated in the following:

Samples of low purity exhibit a smaller experimental bulk attempt frequency than predicted by the fit (Eq. 25). This indicates that the charge carrier concentration may be overestimated for these samples.

The total domain indeed has similar oxygen vacancy self-diffusion coefficients compared to bulk measurements; however, most experiments show a higher activation enthalpy leading to higher experimental attempt frequencies obviously due to the grain boundary contribution.[100]

High concentrations of impurities that associate with the oxygen vacancies lead to a significant increase in activation enthalpy and experimental attempt frequency especially at low temperatures where dopants and oxygen vacancies possibly associate. This can be seen by comparing measurements from this work with the bulk domain of Wang *et al.*[100]

With increasing temperature the charge carrier concentration increases, one example is given by Kamiya *et al.*[103] whose low-temperature regime might show bulk dominated properties indicated by the low experimental attempt frequency. Brugner *et al.*[102] show similar high $\overline{v}_{\mathrm{exp},V_O^{\bullet\bullet}}$ and ΔH_a at high temperature for both single crystals and polycrystalline samples indicating that at high temperatures a reduction-dominated region exists. In this work, a constant charge carrier concentration was used, leading for a reduction-dominated region to an overestimated increase in oxygen vacancy self-diffusion coefficient. Consequently, the resulting experimental attempt frequency is too high.

The example of pure ceria emphasizes the difficulties in measuring the experimental attempt frequency. While calculations are often performed in defect-poor (or periodic) materials, creating these materials experimentally is challenging. Here, the experimental bulk attempt frequencies for stoichiometric ceria are the best values for comparison and indeed agree with the calculated attempt frequency.

4.6 Experimental values for doped ceria

For the bulk of Sm and Y doped ceria,[115,118,131,132] a similar fit of the macroscopic, experimental attempt frequencies using Eqs. 1 and 2 would lead to an increase in the experimental attempt frequency with increasing dopant fraction. Here, overestimated attempt frequencies for small dopant fractions[131,132] were neglected due to an unknown number of charge carriers because of additional impurities.

However, despite the considerations above, comparing the attempt frequency for doped ceria is more difficult, since we cannot use the classical Einstein equation (Eq. 1) as there are many defects, which will interact. Moreover, in doped ceria, a variety of possible defect configurations exists leading to a distribution of different jump environments with a distribution of migration

energies and possibly different local attempt frequencies. In contrast, in experiments, the linear interpolation of the conductivity with temperature in the Arrhenius plot gives only a single value for the attempt frequency and for the activation enthalpy. Comparing a single fit value with the actually present distribution is not trivial. Beyond that, the apparent value of the attempt frequency obtained by fitting is directly influenced by the distribution of migration energies.

This dependency can be shown in a simple model: We consider a highly ordered, fluorite structured crystal, half of the migration energies are 0.5 eV and the other half is larger by a value *b*. Both jump environments appear alternating. Now we let a single oxygen vacancy jump through the crystal. Each jump has the same attempt frequency. To simulate the ionic conductivity we can use kinetic Monte Carlo simulations according to previous calculations.[20,126] In Fig. 9(a), the oxygen ion conductivity for the simple model was calculated between 500 and 700 K for different *b*-values. All linear regressions of the simulated conductivities, naively based on Eqs. 1 and 2, show a good fit.

The fit parameters are the apparent attempt frequency and the apparent activation enthalpy shown in Fig. 9(b,c). The resulting activation enthalpy is about 0.5 eV + *b*. Therefore, the activation enthalpy is strongly influenced by the higher migration energy. Although we always use the same attempt frequency in the kinetic Monte Carlo simulations, the apparent attempt frequency increases for higher migration energies. For high *b*-values only the higher migration energy determines the ionic conductivity and the lower migration barrier is passed in a considerably small amount of time. Therefore, the covered distance is doubled, which appears here in the doubled attempt frequency. The effect is already mentioned in literature. Wang *et al.*[100] explains the increase in pre-exponential factor for high dopant fractions with the migration distance after each rate-controlling jump, which increases beyond the lattice jump distance of the oxygen vacancy. This simple example shows that the experimental attempt frequency is strongly influenced by the distribution of migration energies.

Therefore, we have to perform kinetic Monte Carlo simulations, which include different attempt frequencies for different ionic configurations, to compare calculated attempt frequencies with experimental attempt frequencies for doped ceria. For Sm doped ceria and the calculated configuration-dependent attempt frequencies, we will report on kinetic Monte Carlo simulations in a subsequent paper.

5 Conclusion

We calculated the attempt frequency for an oxygen ion jump in pure and Sm doped ceria. The convergence of the phonon mesh was shown pointing out that the common reduction to the Gamma point is not sufficient to calculate the attempt frequency. The resulting attempt frequency for the constant volume case in harmonic approximation $\left(1.47 \cdot 10^{12} \text{ s}^{-1}\right)$ and constant pressure case in quasi-harmonic approximation $\left(7.67 \cdot 10^{12} \text{ s}^{-1}\right)$ for pure ceria at 900 K is in agreement with common literature estimates and experiments. Experimental attempt frequencies scatter within several orders of magnitude while they are probably based
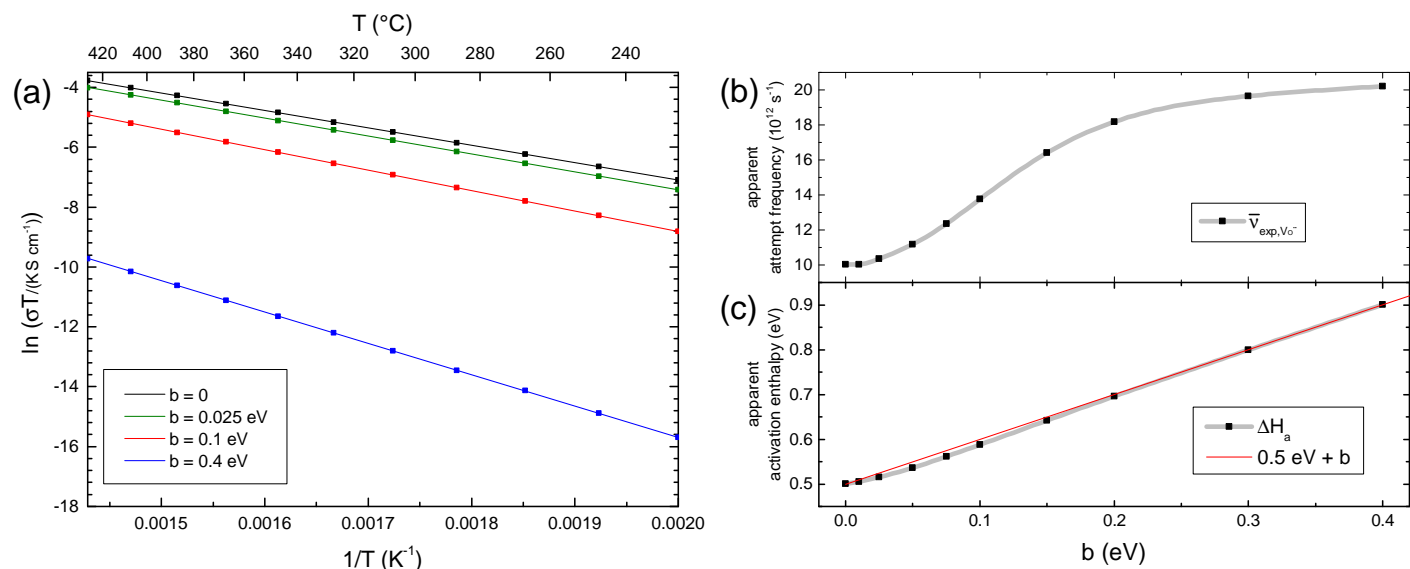
This journal is © the Owner Societies 2017

Phys. Chem. Chem. Phys., 2017, **19**, 9957| 1–17 | 13

Fig. 9 The (a) ionic conductivity for the simple model and regression according to Eqs. 1 and 2. The fit parameters are the (b) apparent oxygen vacancy attempt frequency and (c) the apparent activation enthalpy.

on the same elemental frequency for a jump process. The calculated attempt frequency is unaffected by doping with a single Sm ion at the migration edge while a Sm-Sm edge exhibits a significantly larger attempt frequency. Calculated attempt frequencies of doped ceria should only be compared with experimental attempt frequencies by performing kinetic Monte Carlo simulations.

Acknowledgements

Appendix: Experimental Details

Samples were prepared by dissolving cerium (III) nitrate hexahydrate (99.9%, Chempur) and citric acid (VWR International, 2.5 equivalent) in water. During mixing for several hours at 50 °C the sol-gel transformation occurred. The temperature was increased to 350 °C where the produced foam was dried for three hours and subsequently calcined for four hours at 1000 °C. The calcined powder was dry milled in a planetary mill, uniaxially pressed to disks (10 mm in diameter and 2 mm thick) and sintered in air at 1400 °C for 24 hours. The composition was successfully verified using X-Ray diffraction (Theta-Theta diffractometer, STOE, Darmstadt, Germany). Density measurements according to the Archimedes method gave high densities around 98% of the theoretical value. For impedance measurements, samples were coated with platinum paste and connected with platinum wire. Impedance spectroscopy measurements were performed in air using a two-point geometry (Solatron 1260) with frequencies between 10^7 and $7 \cdot 10^{-2}$ Hz. The bulk semicircle was identified

according to literature.[100] The depressed bulk semicircle in the complex impedance plot was analyzed using an equivalent circuit composed of an RQ-element with the constant phase element Q. The ionic conductivity was calculated according to $\sigma = \frac{d}{AR}$ with the sample thickness d and the area A.

References

1 M. Panhans and R. Blumenthal, *Solid State Ionics*, 1993, **60**, 279–298.

2 K. Eguchi, T. Setoguchi, T. Inoue and H. Arai, *Solid State Ionics*, 1992, **52**, 165–172.

3 G. Murch, *Solid State Ionics*, 1982, **7**, 177–198.

4 M. Nakayama and M. Martin, *Physical Chemistry Chemical Physics*, 2009, **11**, 3241–3249.

5 L. T. Kong and L. J. Lewis, *Physical Review B*, 2006, **74**, 073412.

6 W. D. Kingery, H. K. Bowen and D. R. Uhlmann, *Introduction to ceramics*, Wiley, New York, 2nd edn, 1976.

7 H. Hayashi, *Solid State Ionics*, 2000, **131**, 281–290.

8 H. Inaba, *Solid State Ionics*, 1999, **122**, 95–103.

9 A. Gotte, D. Spangberg, K. Hermansson and M. Baudin, *Solid State Ionics*, 2007, **178**, 1421–1427.

10 A. Tarancón, A. Morata, F. Peiró and G. Dezanneau, *Fuel Cells*, 2011, **11**, 26–37.

11 M. Burbano, S. Nadin, D. Marrocchelli, M. Salanne and G. W. Watson, *Physical Chemistry Chemical Physics*, 2014, **16**, 8320–8331.

12 L. Sun, D. Marrocchelli and B. Yildiz, *Nature communications*, 2015, **6**, 6294.

13 A. Murray, G. Murch and C. Catlow, *Solid State Ionics*, 1986, **18-19**, 196–202.

14 R. Krishnamurthy, Y.-G. Yoon, D. J. Srolovitz and R. Car, *Journal of the American Ceramic Society*, 2004, **87**, 1821–

1830.

15 R. Pornprasertsuk, P. Ramanarayanan, C. B. Musgrave and F. B. Prinz, *Journal of Applied Physics*, 2005, **98**, 103513.

16 R. Pornprasertsuk, J. Cheng, H. Huang and F. B. Printz, *Solid State Ionics*, 2007, **178**, 195–205.

17 S. Grieshammer, T. Zacherle and M. Martin, *Physical Chemistry Chemical Physics*, 2013, **15**, 15935–15942.

18 P. P. Dholabhai, S. Anwar, J. B. Adams, P. Crozier and R. Sharma, *Journal of Solid State Chemistry*, 2011, **184**, 811–817.

19 M. Mogensen, *Solid State Ionics*, 2000, **129**, 63–94.

20 S. Grieshammer, B. O. H. Grope, J. Koettgen and M. Martin, *Physical Chemistry Chemical Physics*, 2014, **16**, 9974.

21 H. Tuller and A. Nowick, *Journal of Physics and Chemistry of Solids*, 1977, **38**, 859–867.

22 R. Farra, M. García-Melchor, M. Eichelbaum, M. Hashagen, W. Frandsen, J. Allan, F. Girgsdies, L. Szentmiklósi, N. López and D. Teschner, *ACS Catalysis*, 2013, **3**, 2256–2268.

23 M. V. Ganduglia-Pirovano, J. L. F. Da Silva and J. Sauer, *Physical Review Letters*, 2009, **102**, 026101.

24 M. Nakayama, H. Ohshima, M. Nogami and M. Martin, *Physical Chemistry Chemical Physics*, 2012, **14**, 6079.

25 P. R. L. Keating, D. O. Scanlon, B. J. Morgan, N. M. Galea and G. W. Watson, *The Journal of Physical Chemistry C*, 2012, **116**, 2443–2452.

26 T. Zacherle, A. Schriever, R. A. De Souza and M. Martin, *Physical Review B*, 2013, **87**, 134104.

27 J. J. Plata, A. M. Márquez and J. F. Sanz, *The Journal of Physical Chemistry C*, 2013, **117**, 25497–25503.

28 S. Arrhenius, *Zeitschrift für Physikalische Chemie*, 1889, **4**, 226–248.

29 M. Trautz, *Chemistry*, 1916, **96**, 1–28.

30 W. C. Lewis, *Journal of the Chemical Society*, 1918, **113**, 471.

31 H. Eyring, *The Journal of Chemical Physics*, 1935, **3**, 107.

32 G. H. Vineyard, *Journal of Physics and Chemistry of Solids*, 1957, **3**, 121–127.

33 R. D. Present, *Proceedings of the National Academy of Sciences*, 1955, **41**, 415–417.

34 V. Pontikis, *Diffusion in materials*, Kluwer Acad. Publ, Dordrecht, 1990, vol. 179, p. 37.

35 H. A. Kramers, *Physica*, 1940, **7**, 284–304.

36 M. Toller, G. Jacucci, G. DeLorenzi and C. P. Flynn, *Physical Review B*, 1985, **32**, 2082–2095.

37 G. De Lorenzi, G. Jacucci and C. P. Flynn, *Physical Review B*, 1987, **36**, 9461–9468.

38 M. Marchese, G. Jacucci and C. P. Flynn, *Physical Review B*, 1987, **36**, 9469–9481.

39 M. Marchese and C. P. Flynn, *Physical Review B*, 1988, **38**, 12200–12207.

40 J. H. Harding, *Reports on Progress in Physics*, 1990, **53**, 1403–1466.

41 P. Hänggi and M. Borkovec, *Reviews of Modern Physics*, 1990, **62**, 251–341.

42 S. Glasstone, K. J. Laidler and H. Eyring, *The theory of rate processes: the kinetics of chemical reactions, viscosity, diffusion and electrochemical phenomena*, McGraw-Hill Book Company, inc, 1941.

43 H. Eyring, *Chemical Reviews*, 1935, **17**, 65–77.

44 H. Eyring, S. H. Lin and S. M. Lin, *Basic Chemical Kinetics*, Wiley, New York, 1980.

45 H. Mehrer, *Diffusion in solids: fundamentals, methods, materials, diffusion-controlled processes*, Springer, 2007.

46 C. P. Flynn, *Point defects and diffusion*, Clarendon Press, 1972.

47 E. Whalley, *Advances in Physical Organic Chemistry, 2*, Elsevier, Burlington, 1964, pp. 93–162.

48 J. Philibert, *Atom movements*, Éd. de Physique, Les Ulis, 1991.

49 H. Yildirim, A. Kara, S. Durukanoglu and T. S. Rahman, *Surface Science*, 2006, **600**, 484–492.

50 T. D. B. Jacobs, B. Gotsmann, M. A. Lantz and R. W. Carpick, *Tribology Letters*, 2010, **39**, 257–271.

51 C. H. Bennett and B. J. Alder, *Journal of Physics and Chemistry of Solids*, 1971, **32**, 2111–2122.

52 C. H. Bennett, *Diffusion in solids*, Acad. Press, New York, 1975, p. 73.

53 A. Da Fano and G. Jacucci, *Physical Review Letters*, 1977, **39**, 950–953.

54 S. Rice, *Physical Review*, 1958, **112**, 804–811.

55 H. Glyde, *Reviews of Modern Physics*, 1967, **39**, 373–382.

56 M. Feit, *Physical Review B*, 1972, **5**, 2145–2153.

57 A. D. Le Claire, *Philosophical Magazine*, 1966, **14**, 1271–1284.

58 Y. Ebisuzaki, W. J. Kass and M. O'Keeffe, *The Journal of Chemical Physics*, 1967, **46**, 1373.

59 W. Franklin, *Physical Review*, 1969, **180**, 682–694.

60 D. G. Truhlar, B. C. Garrett and S. J. Klippenstein, *The Journal of Physical Chemistry*, 1996, **100**, 12771–12800.

61 Y. Lu, F. Zheng and P. Zhang, *Journal of Applied Physics*, 2013, **114**, 153507.

62 E. Wimmer, W. Wolf, J. Sticht, P. Saxe, C. B. Geller, R. Najafabadi and G. A. Young, *Physical Review B*, 2008, **77**, 134305.

63 K.-P. Bohnen, R. Heid and B. Renker, *Physical Review Letters*, 2001, **86**, 5771–5774.

64 K.-P. Bohnen, R. Heid and M. Krauss, *Europhysics Letters (EPL)*, 2003, **64**, 104–110.

65 G. Deinzer, G. Birner and D. Strauch, *Physical Review B*, 2003, **67**, 144304.

66 I. I. Mazin, D. J. Singh, M. D. Johannes and M. H. Du, *Physical Review Letters*, 2008, **101**, 057003.

67 A. Shukla, M. Calandra, M. d'Astuto, M. Lazzeri, F. Mauri, C. Bellin, M. Krisch, J. Karpinski, S. M. Kazakov, J. Jun, D. Daghero and K. Parlinski, *Physical Review Letters*, 2003, **90**, 095506.

68 Y. Ma, J. S. Tse, T. Cui, D. D. Klug, L. Zhang, Y. Xie, Y. Niu and G. Zou, *Physical Review B*, 2005, **72**, 014306.

This journal is © the Owner Societies 2017

Phys. Chem. Chem. Phys., 2017, **19**, 9957| 1–17 | 15

69 B. Grabowski, T. Hickel and J. Neugebauer, *Physical Review B*, 2007, **76**, 024309.

70 L. T. Kong and L. J. Lewis, *Physical Review B*, 2008, **77**, 165422.

71 M. Mantina, L. Q. Chen and Z. K. Liu, *Defect Diffus. Forum (Defect and Diffusion Forum)*, 2009, **294**, 1–13.

72 O. N. Bedoya-Martínez and G. Roma, *Physical Review B*, 2010, **82**, 134115.

73 M. Mantina, Y. Wang, R. Arroyave, S. L. Shang, L. Q. Chen and Z. K. Liu, *Journal of Physics: Condensed Matter*, 2012, **24**, 305402.

74 A. S. Fedorov and A. F. Sadreev, *Physical Status Solidi B*, 2009, **246**, 2598–2601.

75 A. A. Maradudin, *Theory of lattice dynamics in the harmonic approximation. 2. ed*, Academic Press, New York, N.Y, 1971, vol. 3.

76 P. G. Sundell, M. E. Björketun and G. Wahnström, *Physical Review B*, 2007, **76**, 094301.

77 K. Toyoura, Y. Koyama, A. Kuwabara, F. Oba and I. Tanaka, *Physical Review B*, 2008, **78**, 214303.

78 J. P. Perdew, K. Burke and M. Ernzerhof, *Physical Review Letters*, 1997, **78**, 1396.

79 P. E. Blöchl, *Physical Review B*, 1994, **50**, 17953–17979.

80 G. Kresse and J. Furthmüller, *Physical Review B*, 1996, **54**, 11169–11186.

81 G. Kresse and D. Joubert, *Physical Review B*, 1999, **59**, 1758–1775.

82 S. L. Dudarev, G. A. Botton, S. Y. Savrasov, C. J. Humphreys and A. P. Sutton, *Physical Review B*, 1998, **57**, 1505–1509.

83 J. Hooper, A. Ismail, J. B. Giorgi and T. K. Woo, *Physical Chemistry Chemical Physics*, 2010, **12**, 12969.

84 P. P. Dholabhai, J. B. Adams, P. Crozier and R. Sharma, *Physical Chemistry Chemical Physics*, 2010, **12**, 7904.

85 H. Jonsson, G. Mills and K. M. Jacobsen, *Classical and quantum dynamics in condensed phase simulations*, World Scientific, Singapore, 1998, pp. 385–404.

86 M. Lumeij, J. Koettgen, M. Gilleßen, T. Itoh and R. Dronskowski, *Solid State Ionics*, 2012, **222-223**, 53–58.

87 G. Henkelman, B. P. Uberuaga and H. Jónsson, *The Journal of Chemical Physics*, 2000, **113**, 9901.

88 K. Parlinski, Z. Q. Li and Y. Kawazoe, *Physical Review Letters*, 1997, **78**, 4063–4066.

89 A. Franke and E. Pehlke, *Physical Review B*, 2009, **79**, 235441.

90 J. Hafner, *Journal of Computational Chemistry*, 2008, **29**, 2044–2078.

91 D. E. Jiang and E. A. Carter, *Physical Review B*, 2003, **67**, 214103.

92 D. F. Johnson and E. A. Carter, *The Journal of Physical Chemistry C*, 2010, **114**, 4436–4444.

93 P. Ágoston and K. Albe, *Physical Chemistry Chemical Physics*, 2009, **11**, 3226.

94 Y. Mishin, M. R. Sørensen and A. F. Voter, *Philosophical Magazine A*, 2001, **81**, 2591–2612.

95 A. Suzuki and Y. Mishin, *Interface Science*, 2003, **11**, 131–148.

96 I. Riess, M. Ricken and J. Nölting, *Journal of Solid State Chemistry*, 1985, **57**, 314–322.

97 T. Hisashige, Y. Yamamura and T. Tsuji, *Journal of Alloys and Compounds*, 2006, **408–412**, 1153–1156.

98 H. Hayashi, M. Kanoh, C. J. Quan, H. Inaba, S. Wang, M. Dokiya and H. Tagawa, *Solid State Ionics*, 2000, **132**, 227–233.

99 H. Inaba and H. Tagawa, *Journal of the Ceramic Society of Japan*, 1998, **106**, 272–278.

100 D. Y. Wang and A. S. Nowick, *Journal of Solid State Chemistry*, 1980, **35**, 325–333.

101 J. M. Floyd, *Indian J. Tech.*, 1973, **11**, 589–594.

102 F. S. Brugner and R. N. Blumenthal, *Journal of the American Ceramic Society*, 1971, **54**, 57.

103 M. Kamiya, E. Shimada, Y. Ikuma, M. Komatsu and H. Haneda, *Journal of The Electrochemical Society*, 2000, **147**, 1222.

104 M. Kamiya, E. Shimada and Y. Ikuma, *Journal of the Ceramic Society of Japan*, 1998, **106**, 1023–1026.

105 I. K. Naik and T. Y. Tien, *Journal of Physics and Chemistry of Solids*, 1978, **39**, 311–315.

106 H. L. Tuller, *Journal of The Electrochemical Society*, 1979, **126**, 209.

107 M. Martin, T. Zacherle, A. Schriever, R. A. d. Souza and S. Grieshammer, *ECS Transactions*, 2013, **57**, 2405–2410.

108 R. N. Blumenthal, P. W. Lee and R. J. Panlener, *Journal of The Electrochemical Society*, 1971, **118**, 123.

109 G. E. Murch, *Philosophical Magazine A*, 1982, **45**, 685–692.

110 E. Ruiz-Trejo, J. D. Sirman, Y. M. Baikov and J. A. Kilner, *Solid State Ionics*, 1998, **113-115**, 565–569.

111 P. S. Manning, J. D. Sirman, R. A. De Souza and J. A. Kilner, *Solid State Ionics*, 1997, **100**, 1–10.

112 H. J. Avila-Paredes, P. Jain, S. Sen and S. Kim, *Chemistry of Materials*, 2010, **22**, 893–897.

113 P. Jain, H. J. Avila-Paredes, C. Gapuz, S. Sen and S. Kim, *The Journal of Physical Chemistry C*, 2009, **113**, 6553–6560.

114 K. Fuda, *Journal of Physics and Chemistry of Solids*, 1984, **45**, 1253–1257.

115 M. G. Bellino, D. G. Lamas and N. E. Walsöe de Reca, *Advanced Functional Materials*, 2006, **16**, 107–113.

116 U. Anselmi-Tamburini, F. Maglia, G. Chiodelli, A. Tacca, G. Spinolo, P. Riello, S. Bucella and Z. A. Munir, *Advanced Functional Materials*, 2006, **16**, 2363–2368.

117 K. Singh, S. A. Acharya and S. S. Bhoga, *Ionics*, 2007, **13**, 429–434.

118 Z. Zhan, T.-L. Wen, H. Tu and Z.-Y. Lu, *Journal of The Electrochemical Society*, 2001, **148**, A427.

119 W. Huang, *Solid State Ionics*, 1997, **100**, 23–27.

120 C. Peng, Y. Zhang, Z. W. Cheng, X. Cheng and J. Meng, *Journal of Materials Science: Materials in Electronics*, 2002, **13**, 757–762.

121 J. van Herle, T. Horita, T. Kawada, N. Sakai, H. Yokokawa and M. Dokiya, *Journal of the European Ceramic Society*, 1996, **16**, 961–973.

122 S. P. Harvey, R. A. De Souza and M. Martin, *Energy Environ. Sci.*, 2012, **5**, 5803–5813.

123 P. Manning, *Solid State Ionics*, 1996, **93**, 125–132.

124 K. Huang, M. Feng and J. B. Goodenough, *Journal of the American Ceramic Society*, 1998, **81**, 357–362.

125 R. O. Fuentes and R. T. Baker, *Journal of Power Sources*, 2009, **186**, 268–277.

126 B. O. H. Grope, T. Zacherle, M. Nakayama and M. Martin, *Solid State Ionics*, 2012, **225**, 476–483.

127 G. Kemeny and B. Rosenberg, *Nature*, 1973, **243**, 400–401.

128 Y.-J. Wang, M. Zhang, L. Liu, S. Ogata and L. H. Dai, *Physical Review B*, 2015, **92**, 174118.

129 W. Meyer and H. Neldel, *Zeitschrift für technische Physik*, 1937, **18**, 588–593.

130 G. Kemeny and S. D. Mahanti, *Proceedings of the National Academy of Sciences of the United States of America*, 1975, **72**, 999–1002.

131 D. Wang, D. Park, J. Griffith and A. Nowick, *Solid State Ionics*, 1981, **2**, 95–105.

132 C. Tian and S.-W. Chan, *MRS Proceedings*, 1998, **548**, 629–634.

This journal is © the Owner Societies 2017

Phys. Chem. Chem. Phys., 2017, **19**, 9957| 1–17 | 17